Polychaetoid/ZO-1 strengthens cell junctions under tension while localizing differently than core adherens junction proteins

Mark Peifer[a,*], Anja Schmidt[a], Tara Finegan[b,†], Matthias Häring[c,d,e,f,†], Deqing Kong[g,†], Alexander G. Fletcher[h], Zuhayr Alam[a], Jörg Grosshans[g], and Fred Wolf[c,d,e,f]

[a]Department of Biology, University of North Carolina at Chapel Hill, Chapel Hill, NC 27599-3280; [b]Department of Biology, University of Rochester, Rochester, New York 14627-0211; [c]Göttingen Campus Institute for Dynamics of Biological Networks, Georg August University, 37075 Göttingen, Germany; [d]Max Planck Institute for Dynamics and Self-Organization, 37077 Göttingen, Germany; [e]Max Planck Institute for Multidisciplinary Sciences, 37075 Göttingen, Germany; [f]Institute for Dynamics of Complex Systems, Georg August University, 37077 Göttingen, Germany; [g]Department of Biology, Philipps University, 35043 Marburg, Germany; [h]School of Mathematics and Statistics and Bateson Centre, University of Sheffield, Sheffield S10 2TN, United Kingdom

ABSTRACT During embryonic development, dramatic cell shape changes and movements reshape the embryonic body plan. These require robust but dynamic linkage between the cell–cell adherens junctions and the force-generating actomyosin cytoskeleton. Our view of this linkage has evolved, and we now realize linkage is mediated by mechanosensitive multi-protein complexes assembled via multivalent connections. Here we combine genetic, cell biological, and modeling approaches to define the mechanism of action and functions of an important player, *Drosophila polychaetoid*, homologue of mammalian ZO-1. Our data reveal that Pyd reinforces cell junctions under elevated tension, and facilitates cell rearrangements. Pyd is important to maintain junctional contractility and in its absence cell rearrangements stall. We next use structured illumination microscopy to define the molecular architecture of cell–cell junctions during these events. The cadherin–catenin complex and Cno both localize to puncta along the junctional membrane, but are differentially enriched in different puncta. Pyd, in contrast, exhibits a distinct localization to strands that extend out from the region occupied by core junction proteins. We then discuss the implications for the protein network at the junction–cytoskeletal interface, suggesting different proteins localize and function in distinct ways, perhaps in distinct subcomplexes, but combine to produce robust connections.

INTRODUCTION

One fundamental property of animal cells is their ability to change shape and move. This depends on force generation, with the acto-myosin cytoskeleton playing a prominent role. However, for force to be translated into cell shape change and movement, the cytoskel-eton must be anchored at the plasma membrane. This occurs at cell–cell and cell–matrix junctions, which also serve as signal transduction hubs for sensing and transducing mechanical force and chemical signals (Ladoux and Mege, 2017). One challenge for our

Abbreviations used: AJs, adherens junctions; AP, anterior/posterior; Arm, Armadillo; Baz, Bazooka; Cno, Canoe; DV, dorsal/ventral; Ecad, E-cadherin; GFP, green fluorescent protein; mCH, monomeric Cherry; M/Z mutants, maternal/zy-gotic mutants; Pyd, Polychaetoid; RNAi, RNA interference; TCJs, tricellular junc-tions; WT, wild-type.

field is to define the machinery and mechanisms that link cell–cell adherens junctions (AJs) to the cytoskeleton, allowing tissues to change shape during the complex events of embryonic morphogenesis without disrupting tissue architecture.

Our understanding of the nature of this linkage evolved rapidly over the last two decades. The central role of transmembrane cadherins and their cytoplasmic partners β- and α-catenin in mediating adhesion was defined early on. This initially suggested a simple linear connection to actin, via the ability of α-catenin to bind actin. However, new data made this picture increasingly complex, with the addition of many additional proteins at the AJ–cytoskeletal interface and the realization that the structure and function of this multiprotein assemblage is altered by applied force, via mechanosensitive feedback loops (Yap *et al.*, 2018; Troyanovsky, 2022). Thus, evolution shaped an exceptionally robust multiprotein machine to accommodate force on AJs during the complex events of morphogenesis (Fernandez-Gonzalez and Peifer, 2022).

We use the fruit fly *Drosophila* as a model, allowing us to combine state-of-the-art genetic and cell biological tools. In *Drosophila*, different proteins occupy distinct places on the spectrum of importance for junctional integrity. The core cadherin–catenin complex and, in most tissues, the polarity protein Bazooka (Baz)/Par3, is essential—its loss disrupts cell adhesion itself (e.g., Cox *et al.*, 1996; Müller and Wieschaus, 1996; Tepass *et al.*, 1996; Uemura *et al.*, 1996; Sarpal *et al.*, 2012). Other proteins, such as Canoe/Afadin, are essential for many morphogenetic movements and support tissue integrity in tissues under tension, but are not essential for adhesion (Boettner *et al.*, 2003; Sawyer *et al.*, 2009, 2011). Finally, some proteins, such as Vinculin (Maartens *et al.*, 2016), Ajuba (Razzell *et al.*, 2018; Rauskolb *et al.*, 2019), or Sidekick (Finegan *et al.*, 2019; Letizia *et al.*, 2019), are not essential for viability or overall morphogenesis, but their loss weakens connections at AJs under tension. In addition, many proteins in the AJ network are complex multidomain proteins—connections linking them are not linear but form a network of multivalent interactions. Thus, one can remove individual domains of important players like Canoe/Afadin (Perez-Vale *et al.*, 2021) or even of α-catenin (Sheppard *et al.*, 2023) without fully disrupting AJ–cytoskeletal connections.

Our current goal is to position *Drosophila* polychaetoid (Pyd), the fly homologue of mammalian Zonula occludens (ZO) proteins, into this network and define its cellular and molecular functions. All family members are complex multidomain proteins with three PDZ domains, SH3 and Guanylate kinase (Guk) domains, an actin binding region, and regions of intrinsic disorder. This multivalent structure allows them to interact with a diverse set of protein partners, including transmembrane proteins such as claudin, occludin, and JAM and adapters such as Canoe/Afadin, as well as actin (Rouaud *et al.*, 2020). We seek to define the roles Pyd plays in the complex events of morphogenesis and in strengthening AJs under tension.

Mammalian ZO-1 and its relatives ZO-2 and ZO-3 are best known for their role in tight junctions, which seal epithelial sheets and preserve barrier function (Umeda *et al.*, 2006). However, they also play a role in AJ establishment in vitro (Itoh *et al.*, 1997; Ikenouchi *et al.*, 2007). The presence of three mammalian family members has made analyzing their roles in morphogenesis challenging. ZO-3 is dispensable. ZO-2 mutants die during gastrulation (Xu *et al.*, 2008), but chimeric embryos, in which the embryo proper is almost exclusively derived from ZO-2 mutant cells, develop normally to adulthood (Xu *et al.*, 2009). ZO-1 mutants gastrulate normally, but die at E10.5 (Katsuno *et al.*, 2008); however, this might also result from defects in extraembryonic tissues. To define the full function of the ZO family, one would need to generate double or triple mutant embryos. This

has not been done, but conditional knockout experiments in the liver (Itoh *et al.*, 2021) and kidney (Itoh *et al.*, 2018) suggest complete or partial redundancy between ZO-1 and ZO-2.

The presence of a single ZO family member in *Drosophila*, Pyd, facilitates analysis of its roles. Pyd was identified via alleles that lead to supernumerary adult bristles (Neel, 1940; Chen *et al.*, 1996); mutants also have adult eye and embryonic tracheal defects (Jung *et al.*, 2006). The gene is complex with 11 potential isoforms and 3 predicted translation start sites, and these original alleles were not null but reduced or altered expression in tissue-specific ways. In 2011, two groups generated alleles completely deleting protein coding sequences (Choi *et al.*, 2011; Djiane *et al.*, 2011). Strikingly, null zygotic mutants were adult viable with defects in bristle number, wing shape, and the female germline, revealing that Pyd is not essential for cell–cell adhesion postembryonic morphogenesis. However, the new alleles allowed the removal of both maternal and zygotic Pyd. This revealed that Pyd, while not essential, is important for high fidelity completion of embryonic morphogenesis. In its absence, 40–60% of embryos die, with defects in the complex movements of head involution and dorsal closure (Choi *et al.*, 2011). However, almost half of the *pyd M/Z* null mutants survived embryogenesis. These data suggest Pyd occupies an interesting place in the spectrum of protein importance for AJ robustness. However, these earlier analyses only examined the latest morphogenetic events, focusing on dorsal closure. Thus, our first goal was to define Pyd's roles during the earlier morphogenetic events when Cno plays important roles. To do so, we assessed localization of other AJ and cytoskeletal proteins, AJ stability, junctional contractility, and cell exchange.

The growing appreciation of the diversity of proteins at the AJ–cytoskeletal interface and their multivalent interactions also raised important questions about the molecular architecture of AJs. AJs are very large molecular assemblies, encompassing hundreds to thousands of copies of E-Cadherin and its cytoplasmic binding partners. Scientists studying cell–matrix junctions led the way, suggesting that these junctions have a layered three-dimensional nanoarchitecture, with different proteins localized to different zones (Case and Waterman, 2015). Analysis of AJ architecture in mammalian epithelial cells using electron microscopy (Efimova and Svitkina, 2018) or elevated resolution light microscopy (e.g., Choi *et al.*, 2016; Bertocchi *et al.*, 2017) also have begun to support models like this, with different AJ or cytoskeletal proteins along the plasma membrane-proximal to membrane-distal axis. However, how AJ architecture evolves during morphogenesis, and how Pyd fits into the picture remain unanswered questions. Thus, our second goal was to use high-resolution microscopy to begin to define the substructure of AJs in vivo during morphogenesis.

RESULTS

Pyd reinforces AJs under elevated tension and facilitates cell rearrangements, but it is less essential for junctional stability than Cno

The multiprotein AJ complex includes proteins whose functions range from essential for adhesion, like the core cadherin–catenin complex, to those important for many morphogenetic movements, like Cno, to those that are dispensable for viability and play reinforcing or tissue-specific roles, like Sdk. Our first goal was to place Pyd's in this network, defining its roles in morphogenesis and comparing them to the roles of Cno.

Unlike *cno*, *pyd* zygotic mutants are viable to adulthood (Seppa *et al.*, 2008; Djiane *et al.*, 2011). However, most maternal/zygotic (M/Z) *pyd* mutants (40–80% depending on the allelic combination)

die as embryos with defects in head involution, dorsal closure, and tracheal development (Jung *et al.*, 2006; Choi *et al.*, 2011), all events occurring near the end of embryonic morphogenesis. During dorsal closure, Pyd plays a role in maintaining a straight leading edge and uniform leading-edge cell shapes, consistent with a role in reinforcing connections between AJs and the leading-edge actomyosin cable. In these phenotypes, M/Z *pyd* mutants resemble zygotic *cno* mutants, which have reduced but not eliminated Cno function (Choi *et al.*, 2011).

Cno plays multiple roles earlier in embryonic development, in events including initial positioning of AJs (Choi *et al.*, 2013; Schmidt *et al.*, 2018), mesoderm invagination (Sawyer *et al.*, 2009), and germband elongation (Sawyer *et al.*, 2011). To assess whether Pyd plays roles reinforcing AJ–cytoskeletal connections during these earlier stages, we examined M/Z *pyd* mutants and compared their phenotype to M/Z *cno* mutants. To generate M/Z *pyd* mutant embryos, we crossed homozygous mutant females with heterozygous *pyd* males and collected embryos from this cross. We distinguished M/Z mutants from paternally rescued siblings by staining with Pyd antibody.

One early role for Cno is in apical constriction of cells in the ventral furrow. By stage 8, the ectoderm should have joined at the midline and mesoderm should be fully internalized (Figure 1A). M/Z *cno* mutants have a fully penetrant defect in this (Sawyer *et al.*, 2009). Consistent with Pyd helping reinforce AJs under tension, ventral furrow invagination was defective in many M/Z *pyd* mutants. However, unlike M/Z *cno* mutants, this phenotype was not fully penetrant. Mesoderm invagination went to completion in 24% of stage 7–9 M/Z *pyd* mutants (*n* = 45 mutant embryos). Fifty-three percent had mild closure defects at the anterior or posterior ends (Figure 1, A vs. B) and only 22% had the severe invagination failure (Figure 1C) seen in M/Z *cno* mutants. Thus, complete loss of Pyd has less severe effects on mesoderm invagination than loss of Cno—it is also less penetrant in its effects than *cnoΔRA*, which lacks Cno's Rap1 binding RA domains. Instead, Pyd loss is more similar in this phenotype to the milder *cnoΔFAB* mutant, which lacks the C-terminal F-actin binding region (Perez-Vale *et al.*, 2021).

We next looked at germband extension, during which planar polarization of AJ and cytoskeletal proteins drives cell intercalation and body axis extension. In M/Z *cno* mutants and in *cno* mutants lacking its Rap1-binding RA regulatory domains, multiple gaps open at AJs under elevated tension: those at AP borders and tricellular junctions (TCJs; Sawyer *et al.*, 2011; Perez-Vale *et al.*, 2021). Cell shapes are also altered in *cno* mutants, with cell elongation and preferential cell alignment along the anterior–posterior (AP) axis. We thus examined cell rearrangements during germband elongation and AJ stability under elevated tension in M/Z *pyd* mutants. We focused on the thoracic and abdominal region during germband extension, which starts in embryonic stage 7 when cells began intercalating.

Two defects were noted in M/Z *pyd* mutants. First, in M/Z *pyd* mutants apical cell shapes became more variable (Figure 1, D vs. E and F), with the appearance of stacks of cells in the lateral ectoderm that were more elongated along the AP axis (Figure 1, E and F, arrows, and G vs. H, arrows). Quantification of cell eccentricity confirmed this cell elongation (Figure 1I). This alteration in cell shape resembled what we saw in *cnoΔRA* mutants (Perez-Vale *et al.*, 2021). Second, occasional apical gaps or more subtle disruptions were observed at TCJs/rosettes or aligned AP borders (Figure 1, J vs. K, yellow or red arrows, respectively). Quantification verified an increase in gaps at stages 7 and 8 (Figure 1L). However, the gaps were not as numerous as those seen after *cno* RNAi (Figure 1M, red

arrows). Instead, the severity of the gap phenotype in M/Z *pyd* mutants was more similar to that seen in the milder *cnoΔFAB* mutant (Perez-Vale *et al.*, 2021). Both of these defects continued at stage 8 in M/Z *pyd* mutants, with the continued presence of stacks of elongated cells (Figure 1, N vs. O, cyan arrows) and an elevated number of gaps (Figure 1O, red arrows, and Figure 1, Q vs. R, insets). However, once again the defects were not as numerous as in embryos mutant for *cnoΔRA*, which lacks the Rap1-binding RA domains and is nearly null in phenotype (Figure 1P, red arrows; Perez-Vale *et al.*, 2021). Thus, the phenotypes of M/Z *pyd* mutants were similar to but quantitatively less severe than those of M/Z *cno* mutants, suggesting that Pyd plays a role in regulating cell shapes and stabilizing AJ–cytoskeletal connections under tension, but its role is more modest than that of Cno.

Pyd helps restrain planar polarity of a subset of AJ proteins, but its loss does not lead to obvious detachment of myosin or actin from AP cell borders

Germband extension is driven in part by reciprocal planar polarization of the actomyosin cytoskeleton to AP borders and junctional proteins to dorsal–ventral (DV) borders. Myosin and F-actin enriched on AP cell borders power myosin-driven contractility and thus T1 cell transitions and formation of multicellular rosettes. Wild-type cadherin–catenin complex proteins and especially Bazooka (Baz)/Par3 are enriched on DV cell borders (Figure 2, A and C", cyan vs. yellow arrows; Bertet *et al.*, 2004; Zallen and Wieschaus, 2004). Intriguingly, Cno is enriched on AP borders while Pyd is enriched at DV borders raising the possibility that each reinforces distinct regions (Manning *et al.*, 2019). Cno is also enriched at TCJs, which are sites of elevated junctional tension as AP borders constrict (Sawyer *et al.*, 2009; Yu and Zallen, 2020). Cno loss leads to broadening of myosin cables at AP borders. In *cno* mutants Arm, Pyd, and especially Baz are reduced on AP borders, strongly elevating their planar polarity (Sawyer *et al.*, 2011; Manning *et al.*, 2019). However, myosin planar polarity is not altered (Sawyer *et al.*, 2011).

We thus examined whether Pyd is important for normal junctional planar polarity. In M/Z *pyd* mutants Baz planar polarity is strongly enhanced (Figure 2, A vs. B, and C" vs. D", cyan vs. yellow arrows; quantified in Figure 2G), and Arm planar polarity is also subtly elevated (Figure 2, C' vs. D'; quantified in Figure 2H). However, in M/Z *pyd* mutants Cno remained somewhat enriched on AP borders (Figure 2, E' vs. F'; quantified in 2I), contrasting with the reversal of Cno planar polarity seen after loss of its regulator Rap1 (Perez-Vale *et al.*, 2023) or deletion of Cno's RA domain (Perez-Vale *et al.*, 2021). Thus, Pyd restrains planar polarity of some but not all AJ proteins. We also examined whether the tight connection of myosin to AJs was disrupted. In wild type, myosin is planar polarized to AP borders during germband extension, and tightly apposed there (Figure 3, A and D, arrows). In M/Z *pyd* mutants, other than places where occasional junction gaps were observed, myosin remained planar polarized and tightly apposed to AP borders (Figure 3, B and E, arrows). This contrasted with the clear separation of myosin cables at AP borders seen in M/Z *cno* mutants (Figure 3C; Sawyer *et al.*, 2011). We also examined F-actin localization. Once again, F-actin did not appear to detach from AP cell borders in M/Z *pyd* mutants (Figure 3F, cyan arrows), except where junctional gaps appeared (Figure 3F, yellow arrows). This contrasts with M/Z *cno* mutants (Sawyer *et al.*, 2011). Together these data suggest Pyd regulates AJ protein planar polarity, but reveal that its role is not as essential as that of Cno. They also reveal that Pyd loss does not lead to myosin detachment from AP borders.
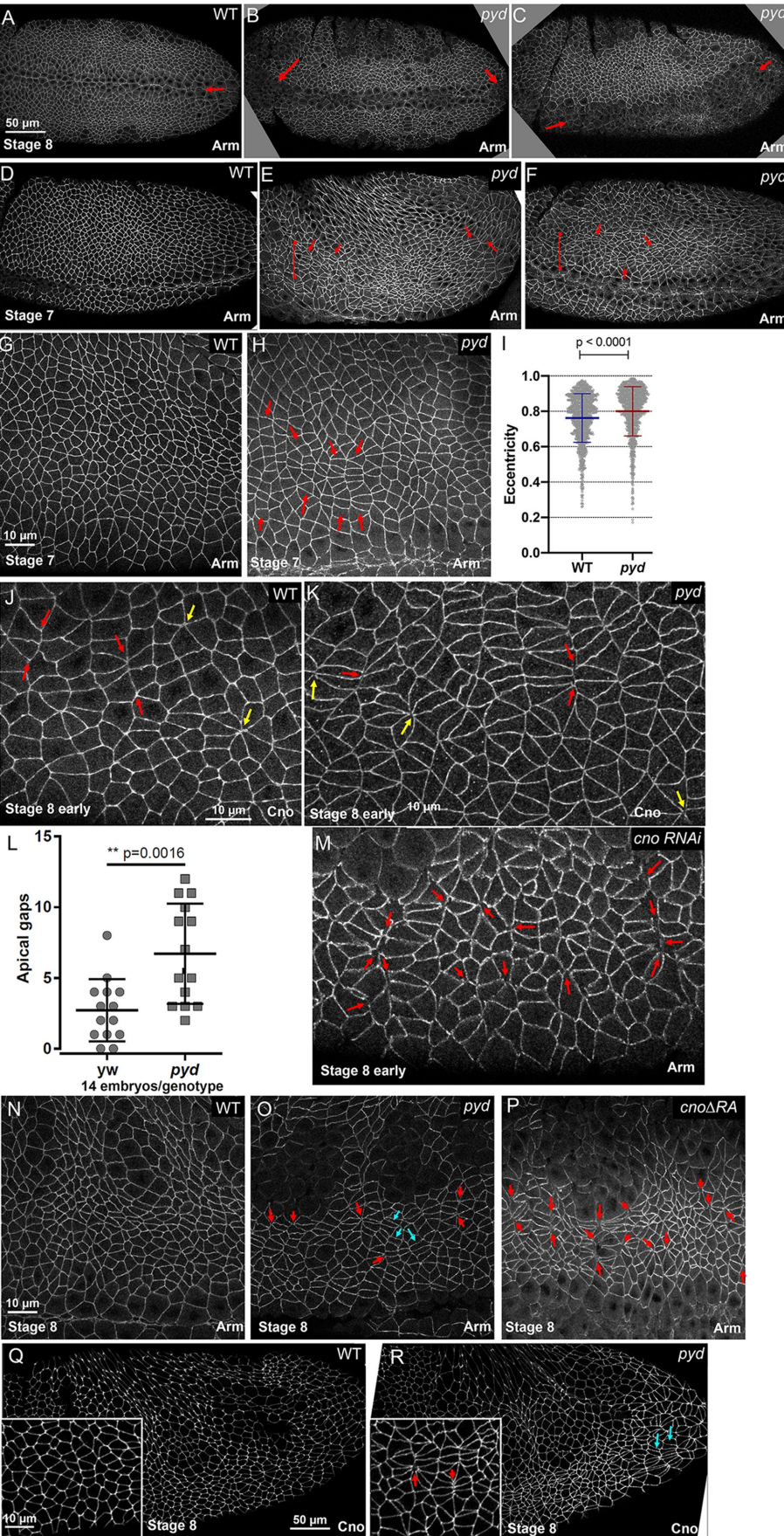
Pyd and Cno are mutually required for one another's enrichment at TCJs

When AJs are put under molecular tension, their connection to the cytoskeleton is strengthened by conformational changes and protein recruitment. For example, Cno is recruited to AJs under tension, including TCJs during germband extension (Figure 4A, arrows; quantified in 4C; Sawyer *et al.*, 2009; Yu and Zallen, 2020), where it is important for TCJ stabilization (Sawyer *et al.*, 2009; Perez-Vale *et al.*, 2021). Pyd is enriched at TCJs in larval wing imaginal discs and was reported to be enriched at TCJs in stage 9–11 embryos (Letizia *et al.*, 2019). Consistent with this, during stage 7 Pyd is modestly enriched at TCJs (Figure 4D, quantified in 4E; ~1.5-fold). Pyd enrichment at TCJs increases as development proceeds, with approximately twofold enrichment at stages 9 and 10 (Supplemental Figure S1, A and C).

FIGURE 1: Pyd facilitates cell rearrangements and reinforces adherens junctions under elevated tension, but is less essential for junctional stability than Cno. Unless noted, in this and subsequent figures embryo images are anterior left and dorsal up. (A–C) Ventral views, stage 8 embryos. (A) In wild type the ventral furrow has closed (arrow). (B, C) In M/Z *pyd* mutants, most embryos have mild (B, arrow) or more severe (C, arrow) defects in ventral furrow closure. (D–H) Stage 7 embryos. (D, G) Wild type. (E, F, H) M/Z *pyd* mutants. In mutants many cells in the ventral ectoderm (brackets) are more elongated along the anterior–posterior axis (E, F arrows). These often form stacks of elongated cells (H, arrows). (I) Quantification of increased cell eccentricity in M/Z *pyd* mutants; significance was determined by Welch's *t* test. *pyd* mutants = 11 embryos, 1212 cells. Wild type = 9 embryos, 1283 cells. (J, K, M) Early stage 8. (J) In wild type cell junctions remain intact, including at aligned AP borders (red arrows) or at rosette centers (yellow arrows). (K) In M/Z *pyd* mutants occasional apical gaps appear in cell junctions at aligned AP borders (red arrows) or at rosette centers (yellow arrows). (L) Quantification of increased frequency of apical junctional gaps in M/Z *pyd* mutants (14 embryos per genotype). The significance was determined by a two-tailed *t* test. (M) Gaps are more frequent in embryos in which Cno function is strongly reduced by RNAi. (N–R) Stage 8. N vs. O and Q vs. R contrast wild type and M/Z *pyd* mutants. In M/Z *pyd* mutants, aligned elongated cells (O, R, cyan arrows) and gaps at apical junctions (O, R inset, red arrows) persist at stage 8. (P) Gaps are also more frequent in *cnoΔRA* mutants (red arrows).

The TCJ-enriched protein Sidekick is important for full TCJ enrichment of Cno in stage 9–11 embryos (Letizia *et al.*, 2019). We thus asked whether Pyd is also required for Cno TCJ enrichment. In M/Z *pyd* mutants, Cno TCJ enrichment at stage 7 was significantly reduced, but not eliminated (Figure 4, A vs. B, arrows; quantified in 4C). Sidekick is also important for Pyd enrichment in imaginal discs (Letizia *et al.*, 2019). We thus wondered whether Cno was similarly required for Pyd TCJ enrichment. We used a validated strong *cno* RNAi line to knockdown Cno maternally and zygotically (Bonello *et al.*, 2018; Manning *et al.*, 2019), and examined effects on Pyd TCJ enrichment. To confirm Cno knockdown, we costained the embryos with Cno antibody. Low levels of Cno were still detectable (Supplemental Figure S1B). Cno knockdown led to gaps at AJs under tension, as previously noted (Manning *et al.*, 2019), and reduced uniform Pyd recruitment at AJs. At stage 8, Pyd TCJ enrichment was largely abolished after *cno* RNAi (Figure 4D, arrows; quantified in 4F), and this continued at stages 9 and 10 (Supplemental Figure S1, B and C). These data are consistent with Pyd being recruited to TCJs under elevated tension, and suggests that the multiple proteins that are enriched at TCJs mutually reinforce one another's recruitment.

M/Z *pyd* mutants have reduced junctional tension

The reduction in Cno TCJ recruitment in M/Z *pyd* mutants and the hyperplanar polarization of Baz to DV borders made us wonder whether loss of Pyd might alter junctional tension. To test this, we used laser cutting to sever the apical junctional cortex in stage 7 embryos, and measured displacement of the TCJs flanking the severed AJ. In wild-type embryos there is a rapid recoil of ~2.4 μm within 10 s (Figure 4, G and I), with a mean initial recoil velocity of ~0.6 μm/s (Figure 4J). These values were reduced in M/Z *pyd* mutants—there was a total recoil of ~1 μm in 10 s (Figure 4, H and I) with a mean initial recoil velocity of ~0.2 μm/s (Figure 4J). There was no significant change in the ratio between the elasticity of the junction and the viscosity coefficient (K; Figure 4K), supporting the idea that the tension on the junctions is affected. Thus, loss of Pyd reduces junctional tension, consistent with the reduction of Cno TCJ recruitment.

Modeling and experimental analysis suggest T1 transitions are slowed or fail in M/Z *pyd* mutants

One of the most striking features of M/Z *pyd* mutants was the appearance of stacks of cells elongated along the AP axis. Similar cell shape defects were observed during germband extension after the loss of other AJ–cytoskeletal linkers (e.g., Sawyer *et al.*, 2011; Tamada *et al.*, 2012; Razzell *et al.*, 2018; Finegan *et al.*, 2019). Planar-polarized myosin contractility at AP borders drives cells into the T1 configuration or into rosettes, which then resolve to extend the DV axis. Our data above reveal that loss of Pyd reduces junctional contractility. We thus wondered whether reducing border contractility could lead to the stacks of cells elongated along the AP axis we observed in M/Z *pyd* mutants.

To test this, we turned to a vertex model of germband extension created to explore cell interface behaviors of the germband during axis extension (Tetley *et al.*, 2016). We adapted an updated version of this germband extension vertex model that includes the extrinsic posterior pulling force of the midgut (Finegan *et al.*, 2019), to test whether reduced contractility recapitulated the cell stacks elongated along the AP axis. We ran the simulation for 400 timesteps, equating to roughly 20 simulated minutes of germband extension (~0.5 min of germband extension per timestep). Starting configurations were the same, and we examined cell shapes and intercalation at 10 min and 20 min of simulated germband extension. In the wild

type, cells effectively intercalated and the germband extended, with cells retaining largely isotropic shapes (Figure 5A, top, and Supplemental Movie 1). In contrast, when "supercontractilty," modeled by a condition where junction shrinkage rate increases as length decreases, was removed to mimic the reduction in contractility seen in *pyd* mutant, cell intercalation was reduced, and the cell shape and arrangement phenotype, with stacks of cells elongated along the AP axis, matched that we see in M/Z *pyd* mutants (Figure 5A, bottom, and Supplemental Movie 2). We next examined whether this reduction in contractility altered the timing of T1 transitions during the simulations. T1 transitions were identified manually by determining the time at which two cells that were not previously contacting established a new junction. This revealed that there was significant delay in the initiation of intercalations in *pyd* mutants, and the distribution of intercalations through simulated time was fundamentally different (Figure 5B; in wild type many transitions happen in the first 5 min, and *pyd* lacks this initial wave). This result demonstrates that the material properties of the tissue are different when hypercontractility of junctions is removed, and that these changes lead to effects on cell shape and T1 transitions.

This modeling suggested the possibility that the reduced AJ contractility we saw in M/Z *pyd* mutants might affect T1 transitions in vivo, in which four cells constrict their AP (vertical) borders to join at a single vertex, and then exit by elongating their DV (horizontal) junctions (Figure 5E). To determine whether M/Z *pyd* mutants have a defect in T1 transitions, we live imaged embryos in stage 7–8 expressing endogenously tagged E-Cadherin GFP (Figure 5, C and D). Movies were then segmented to define cell junctions, and the rate and direction of T1 transitions were analyzed. We found that in wild-type embryos the majority of T1 transitions went directly from the formation of a four-cell vertex into the elongation of the new junction along the AP axis (Figure 5E). Those T1 transitions were scored as direct transitions without an attempt phase. In contrast, when an extending four-cell vertex reversed and returned to a four-cell vertex, only to once again elongate a junction (without defining the direction in which a new junction was being formed), we scored this as an "attempted T1 transition." In wild-type embryos, 58.4% of T1 transitions proceeded directly while 41.6% were scored as attempted T1 transitions (Figure 5G). In contrast, in M/Z *pyd* mutant embryos, only 47.7% of T1 transitions proceeded directly, while 52.3% were scored as attempted T1 transitions (Figure 5, D and G). We then calculated the duration of the attempt phase in wild-type versus M/Z *pyd* mutant embryos. The mean attempt duration in wild-type embryos was 2.1 min while the mean attempt duration was increased in M/Z *pyd* mutants to 3.2 min (Figure 5G). Finally, we scored the fraction of successful T1 transitions. In wild-type embryos, 84% of formed four-cell vertices successfully resulted in a horizontal (AP) elongation of the new border (Figure 5, F and H; $n =$ 551 transitions). However, in *pyd* mutants, only 78% of T1 transitions were successful, while 22% of 4x vertices reverted back (Figure 5, F and H). Together, these data are consistent with the idea that slowed and failed T1 transitions can help explain the stacks of elongated cells we observed in M/Z *pyd* mutant embryos.

Putting this together, our phenotypic data suggest that Pyd reinforces TCJs under elevated tension and restrains hyperplanar polarization of some AJ proteins, but reveal that junctional disruptions are relatively rare in its absence. Cell shapes are altered, with stacks of elongated cells accumulating. Pyd loss reduces but does not eliminate junctional tension, and in doing so reduces TCJ enrichment of Cno. Our modeling suggests that this reduction in junctional tension could impede shrinking of AP borders and intercalation, and our analysis of T1 transitions is consistent with this. This
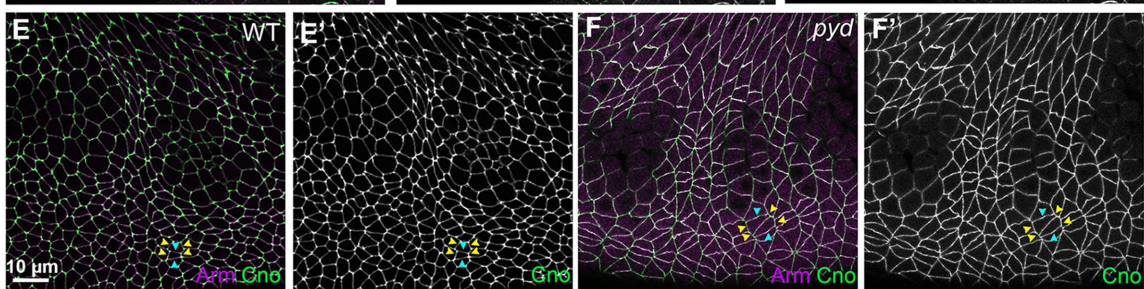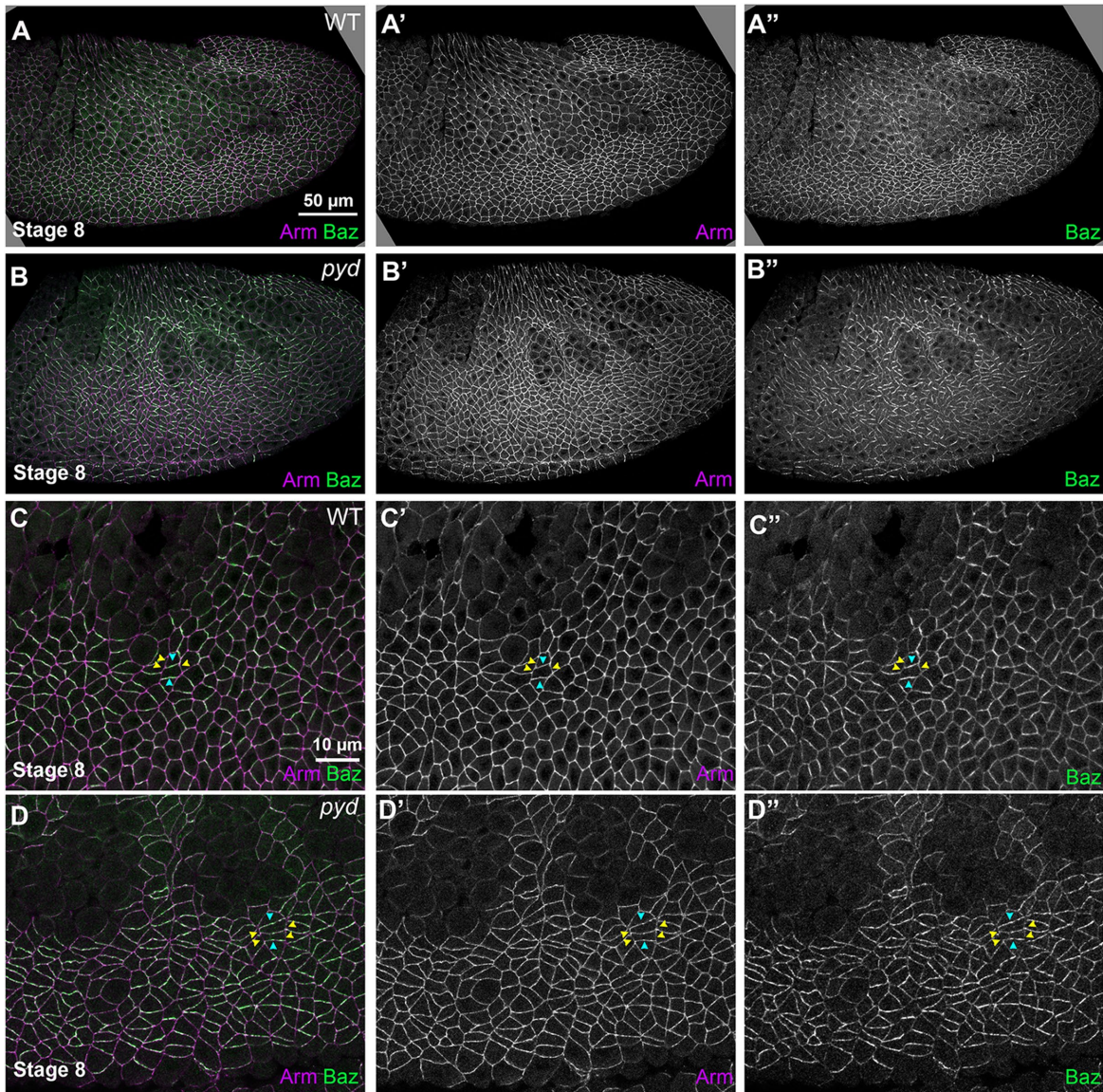
G Baz planar polarity

*** p=0.0004
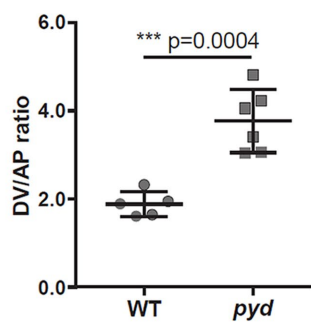
H Arm planar polarity

** p=0.0020
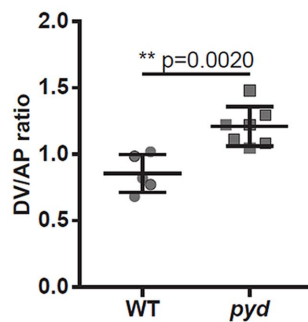
I Cno planar polarity

n.s.

positions Pyd in a new place on the continuum of AJ proteins—less essential than Cno, but more essential than proteins like Sdk or Ajuba, where null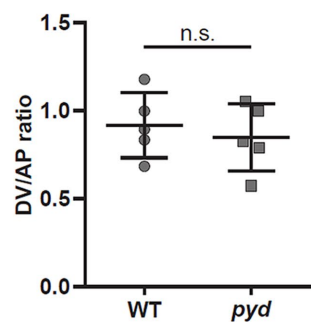 mutants are viable and fertile. It will be important to explore whether some of these differences reflect differential expression of these proteins in different tissues and times, such that the AJ complexes assembled differ in their composition. We saw a hint of this in our earlier work, where the PDZ domain and FAB regions of Cno were differentially required in embryos and the pupal eye (Perez-Vale et al., 2021). Our data also provide mechanistic insights into how Pyd loss alters germband extension.

High-resolution microscopy reveals differential enrichment of the cadherin–catenin complex and Cno in junctional puncta, suggesting AJs have substructure

This continuum of functional importance provided evidence that connections between the cadherin–catenin complex and the cytoskeleton are not the simple, linear connections initially envisaged. We wondered how the supermolecular AJ protein network assembles to create this complex and robust connection. When AJs assemble during cellularization, they form large puncta known as spot AJs (Tepass and Hartenstein, 1994), each of which contains ~1500 cadherin–catenin complexes (McGill et al., 2009). At that stage there are roughly three to eight puncta along each roughly 3–5-µm bicellular junction (BCJ; e.g., Harris and Peifer, 2004; McGill et al., 2009). As gastrulation begins, the punctate character of AJs becomes more complex, and standard confocal microscopy makes junctions look more continuous. To reveal underlying complexity, we used two forms of high-resolution microscopy, structured illumination (SIM) and the Zeiss Airyscan module, to examine AJs at higher lateral resolution, theoretically reaching 100 (SIM)–120 nm (Airyscan).

Both approaches revealed the punctate nature of the core cadherin–catenin complex. As the germband elongates, cell shapes become much less regular, with longer and shorter bicellular borders. At stage 8, SIM revealed small Arm puncta that are tightly aligned along the plasma membrane along BCJs (Figure 6A). We saw a similar distribution of small puncta aligned along BCJs when imaging E-Cadherin GFP using the Zeiss Airyscan detector (Figure 6B), although they were not quite as well resolved. We used the Imaris Spot function to analyze our SIM images. This suggested there are 20–50 Arm puncta per 10 µm of BCJ (Figure 6C; four embryos; 10 borders per embryo). Average puncta size was 0.24 µm, with the extremes of puncta measured extending from 0.15 to 0.4 µm. We next used SIM to explore Arm localization relative to that of Cno. Cno was enriched at AP cell borders (vertical in these images). Cno also localized to small junctional puncta along BCJs (Figure 6, D″ and E″). While the Arm and Cno puncta sometimes overlapped, we were surprised to see that many puncta were differentially enriched for either Arm or Cno (Figure 6, E–E″, red vs. green arrows). Cno was also strongly enriched at TCJs (Figure 6F). To discern relative localization of Arm and Cno at TCJs, we turned down the Cno signal (Figure 6F′). Cno strongly localized to one or more puncta in the center of the TCJ (Figure 6, F′ and F‴, green

arrow, and 6G), with Arm more enriched in puncta around the TCJ periphery (Figure 6, F′ and F″, red arrows, and 6G). Processing our images with Imaris allowed us to visualize the BCJ puncta in 3D; this confirmed the differential enrichment of Arm and Cno in different puncta in the X axis (Figure 6H). However, different chromatic shifts of different fluorophores in the z axis together with differences in z resolution depending on different wavelengths of fluorescence signals mean we cannot draw any conclusions about differential Arm and Cno localization in the Z axis. Thus, while Arm and Cno both localize to AJs, they are differentially enriched in different puncta.

Pyd localizes to strands that span a broader region than the core junctional proteins

We next used SIM imaging to examine Pyd localization relative to that of Arm or Cno. Here the result was even more striking. In using our Pyd antisera in standard confocal imaging, we had been puzzled that its localization was not as "sharply defined" as that of Arm or Cno (e.g., Figure 6, I vs. I′). SIM imaging revealed the reason. Rather than tightly localizing to puncta along bicellular borders, Pyd localized to "strands" over a broader area (Figure 6, J and K). Some overlapped the tighter localization of Arm, but projected membrane distal (Figure 6, J and K, cyan arrows). Other less robust strands projected from the core AJ even further into the membrane-distal zone (Figure 6, J and K, yellow arrows). Because this localization was so surprising, we also imaged Arm and Pyd using the Airyscan module, offering a different way to elevate resolution. This also revealed a broader distribution of Pyd, with strands extending membrane distal from core AJ proteins (Figure 6L). This striking difference was intriguing. To quantify the extent of this difference, we measured the breadth of the signal of Arm, Cno, and Pyd in the x-y plane perpendicular to the junctional plasma membrane (Figure 6M), and then calculated the width of fluorescence signals of all measured borders at a fluorescence intensity of 0.5 (full width, half maximum [FWHM]). The Cno signal appeared to span a slightly broader region than that of Arm, with an FWHM of 280 nm for the Cno signal and 190 nm for the Arm signal (Figure 6N). This is consistent with Arm being directly bound to the cadherin tail and Cno associated by multivalent interactions with actin and other junctional proteins. However, small differences like these could also be due to the fact that the theoretical maximal resolution depends on wavelength, with longer wavelengths leading to lower resolution than shorter wavelengths, and in imaging Arm versus Cno, Cno was visualized using the longer wavelength. Quantifying the span of the Pyd signal confirmed the idea that Pyd extends significantly more plasma membrane distal than Arm or Cno (Figure 6, M and N); the mean FWHM of the Pyd signal was 427 nm compared with 280 nm for the Cno signal and 190 nm for the Arm signal. In this case it is clear that the difference is not solely caused by differences in point spread function, because Pyd, visualized with the 568-nm laser line, was broader than both Arm, visualized using the 488-nm laser line, and Cno, visualized with the 647-nm laser line. Thus, Pyd occupies a region of the AJ complex quite different from the more core AJ proteins.

FIGURE 2: Pyd is required to restrain planar polarity of a subset of AJ proteins. Stage 8 embryos. (A–D) Arm and Baz. (A, C) In wild type Arm is relatively uniform around the cells, while Baz is enriched on DV vs. AP borders (cyan vs. yellow arrowheads). (B, D) In M/Z pyd mutants Arm is subtly reduced at AP borders (yellow arrowheads) and Baz is also reduced, thus enhancing the planar polarity of both. (E) In wild type Cno is subtly enriched on AP vs. DV borders (yellow vs. cyan arrowheads). (F) Cno planar polarity is not substantially altered in M/Z pyd mutants. (G–I) Quantification of Baz, Arm, and Cno planar polarity in wild type and M/Z pyd mutants. Twenty DV and twenty AP borders were measured in five embryos per genotype. Error bars represent SD, and the significance was determined by an unpaired two-tailed t test.
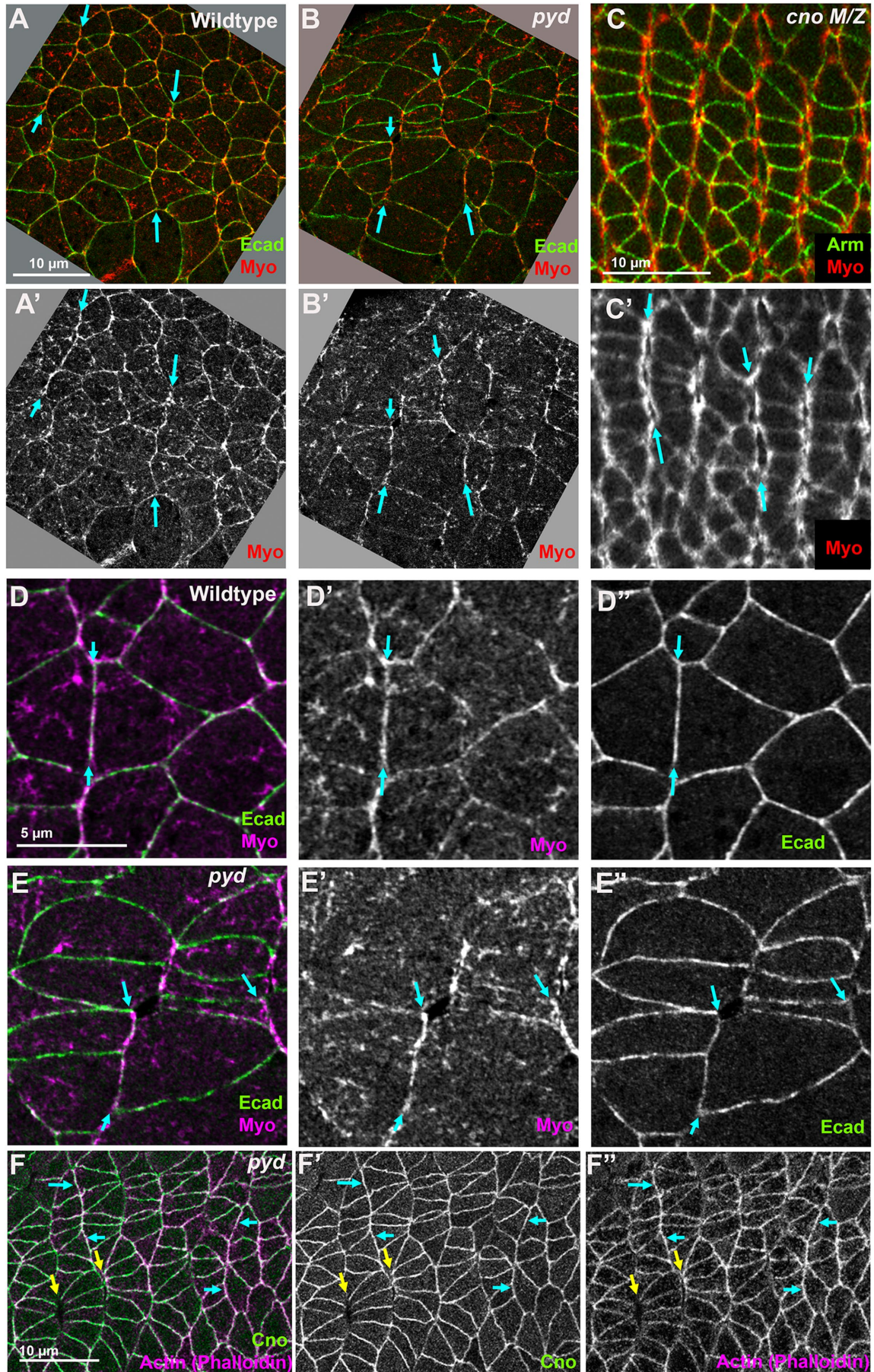
Baz and Arm are differentially enriched in different junctional puncta

Next, we used Airyscan imaging to compare the localization of Arm with that of the apical junctional and polarity protein Bazooka (fly Par). While Baz colocalizes with the cadherin–catenin complex in the spot AJs during cellularization (Harris and Peifer, 2004), Baz then becomes successively more apically enriched (Harris and Peifer, 2005). Our Z stacks of stage 7 embryos were consistent with this, as the Baz signal was considerably brighter apically, while the brightest signal Arm signal was 0.38 µm more basal (Figure 7, A vs. B; brightness not adjusted); however, the issues noted above with resolution in the Z axis make us cautious in interpreting this difference in the z axis. When examined in a single z section, Arm and Baz localizations overlapped along borders in the X-Y axis, but they were differentially enriched in different puncta along BCJs (Figure 7C, red vs. green arrows). Quantification perpendicular to the membrane was consistent with the Baz zone being a bit broader than that of the cadherin–catenin complex and less broad than the distribution of Pyd along the same junctions (Figure 7, D and E), but the caveats noted above make us cautious about interpreting the Arm/Baz difference. Pyd distribution was once again clearly broader than both Arm and Baz. The mean FWHM of the Pyd signal imaged with Airyscan was the same as that imaged with SIM (437 nm), while the mean FWHM of the Baz signal was 276 nm, and that of the Cno signal was 207 nm. Thus, Baz and Arm localize differentially to different puncta along the X-Y plane of bicellular junctions.

Myosin and actin occupy a broader zone along the bicellular junctions than the core AJ proteins

We also were curious about the localization of the cytoskeleton relative to that of the core junctional proteins. During germband elongation, myosin is present in two broad pools: a pool in the apical membrane undergoing waves of periodic condensation, contraction, and dissipation (Rauzi et al., 2010; Fernandez-Gonzalez and Zallen, 2011; Sawyer et al., 2011), and a contractile pool at the AJs (Bertet et al., 2004; Zallen and Wieschaus, 2004). The AJ pool of myosin is planar polarized, with enrichment at AP borders (Figure 7F, cyan arrows), and at multicellular junctions at the center of rosettes (Figure 7F, yellow arrowheads; Bertet et al., 2004; Zallen and Wieschaus, 2004). We used Airyscan imaging to compare the localization of Ecad and myosin. Ecad localized to puncta along each bicellular border (Figure 7, G and G′). Myosin overlapped Ecad but localized to puncta and strands occupying a broader zone that extended membrane distal from Ecad (Figure 7, G and G″). These data are broadly consistent with EM work done in cultured endothelial cells (Efimova and Svitkina, 2018), which also revealed myosin localized membrane distal to the cadherin–catenin complex. We also used phalloidin to visualize F-actin. Similar to myosin, actin localization extended in strands further into the cytoplasm than Cno (Figure 7, H and I, arrows). Thus, the cytoskeletal zone is broader than that of the core junctional proteins.

Using SIM imaging to explore the role of Pyd in AJ molecular architecture

In our final set of experiments, we used SIM imaging to compare AJ architecture in wild-type and in M/Z pyd mutants. In wild type, Arm and Cno localize in overlapping but not identical ways to junctional puncta along bicellular borders (Figure 8, A and B, arrows). This remained essentially unchanged in M/Z pyd mutants (Figure 8, C and D, arrows), except in regions where gaps appeared in junctions (Figure 8C, arrowhead). Arm puncta density along bicellular junctions remained similar (Figure 8I) and Arm puncta remained tightly apposed to the membrane (Figure 8, J and K). We also examined the effect of loss of Pyd on Baz localization. The overlapping but occasionally differential localization of Arm and Baz to different puncta along the bicellular junctions in wild type was not drastically altered in pyd mutants (Figure 8, E and F vs. G and H). However, quantification suggested the possibility that the distribution of Baz was somewhat broader in localization in M/Z pyd mutants relative to wild type (Figure 8, L and M). As a final test of potential roles for Pyd in AJ architecture, we examined whether it affected the mobility of Ecad as assessed by fluorescence recovery after photobleaching (FRAP). We bleached a region of the AJ in embryos expressing Ecad-GFP, and quantified fluorescence recovery (Figure 8N). In wild type, recovery was roughly similar to what others have observed (Cliffe et al., 2004; Greig and Bulgakova, 2021); recovery plateaued after 400–500 s and the mobile fraction was about 75% (Figure 8O). We then repeated this analysis in M/Z pyd mutants. No change was seen in either rate of recovery or mobile fraction (Figure 8O). Thus, Pyd is not essential for many aspects of AJ molecular architecture, but may have effects on Baz localization.
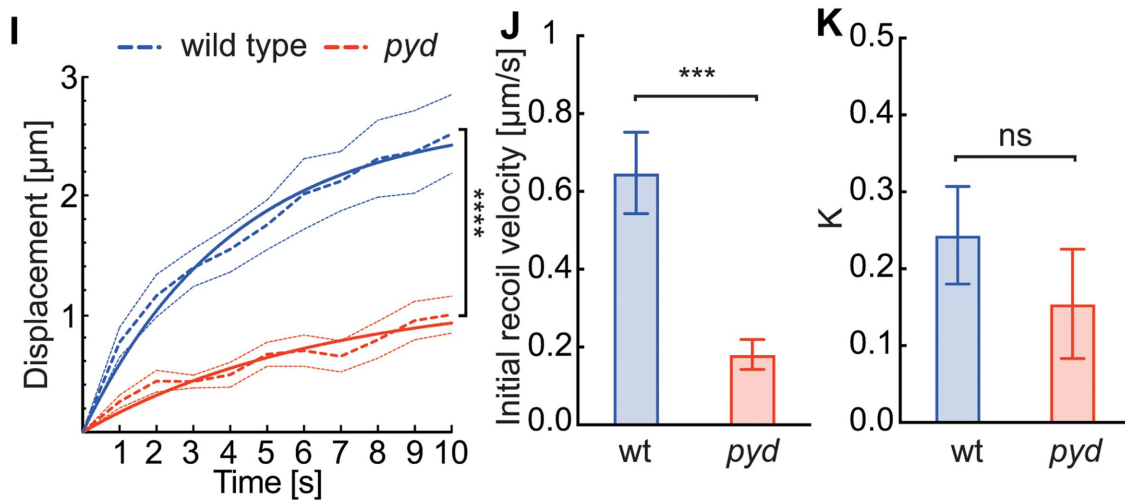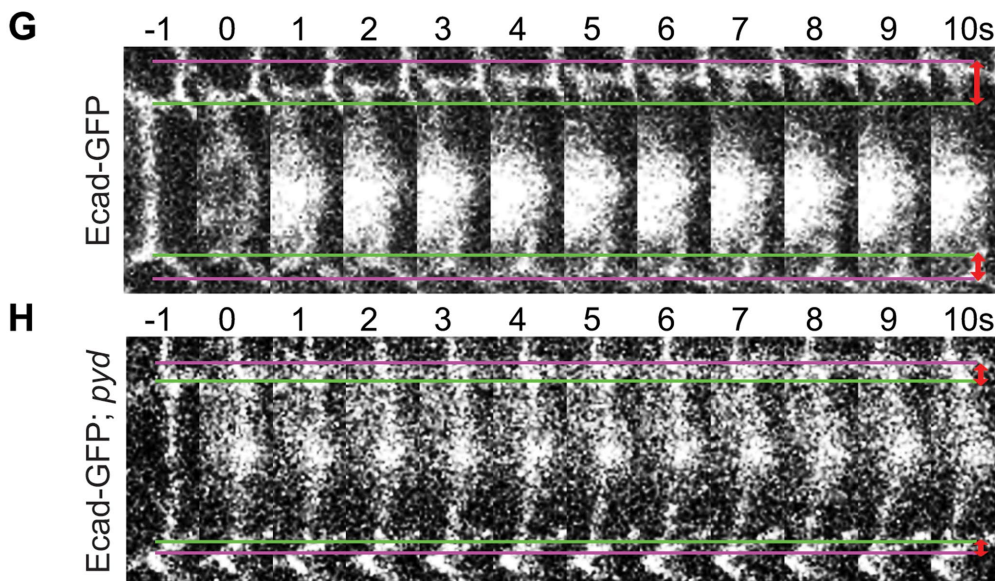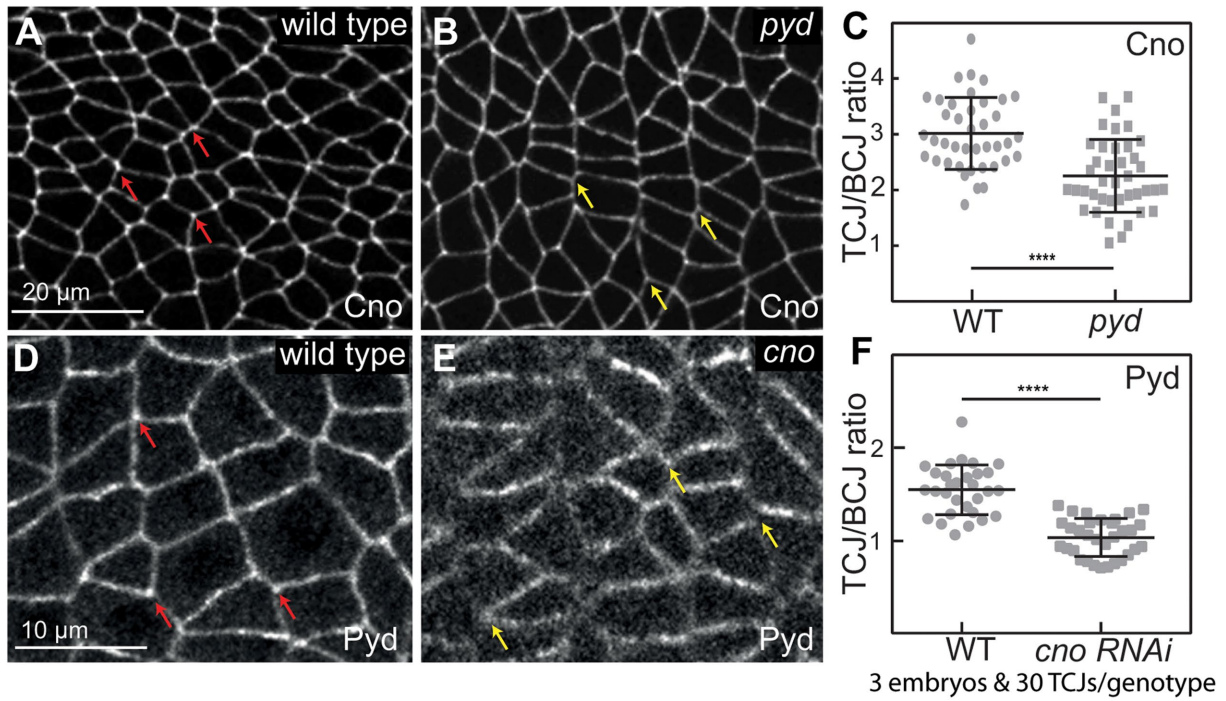
DISCUSSION

Shaping epithelial tissues and organs during embryonic development requires coordinated cell shape change and cell migration, powered by force generated by the actomyosin cytoskeleton exerted on cell–cell and cell–matrix junctions. As a field, we seek to define the underlying molecular mechanisms. The past two decades saw a growing recognition of the complexity of AJ–cytoskeletal connections that allow cell shape change without disrupting tissue integrity (Yap et al., 2018). In this evolving view, simple linear connections mediated by the cadherin–catenin complex were replaced by models involving a robust and multivalent network of proteins. We need to fully define the functions of all the proteins in this network, and to determine the supermolecular structure they assemble at the interface between the cadherin–catenin complex and the cytoskeleton. Here we used *Drosophila* embryonic development as a model, to unravel the function of the scaffold protein Pyd, homologue of human ZO-1, in the robustness of AJ–cytoskeletal connections. In parallel, we used high-resolution microscopy to begin to reveal the layered architecture of the AJ in vivo.

Pyd occupies a new position in the spectrum of proteins mediating AJ–cytoskeletal connections and its phenotypes reveal new complexity in maintaining robustness

In a simple linear model of AJ–cytoskeletal connections, each protein would be equally essential for function. The initial analysis of

---

FIGURE 3: Loss of Pyd does not lead to obvious detachment of myosin from AP cell borders, in contrast with loss of Cno. (A–E) Stage 7 embryos, expressing Ecad-GFP and mCh-Myosin. (A, D) In wild type, junctional myosin is enriched at AP borders (arrows), where it is tightly apposed to junctional Ecad. (B, E) This remains true in M/Z *pyd* mutants (arrows), except where there are junctional gaps. (C) In contrast, in M/Z *cno^{R2}* null mutants, Myosin cables separate at AP borders (arrows). (F) Stage 7. F-actin, as using using Phalloidin, does not detach from AP borders in M/Z *pyd* mutants (cyan arrows), except places where junctions have detached as marked by Cno (yellow arrows).

A wild type — Cno; B *pyd* — Cno; C Cno TCJ/BCJ ratio WT vs *pyd* ****; D wild type — Pyd; E *cno* — Pyd; F Pyd TCJ/BCJ ratio WT vs *cno RNAi* ****; 3 embryos & 30 TCJs/genotype; G Ecad-GFP; H Ecad-GFP; *pyd*; I Displacement [μm] vs Time [s], wild type, *pyd* ****; J Initial recoil velocity [μm/s] wt vs *pyd* ***; K K wt vs *pyd* ns

Ecad, Arm, and α-catenin fit this simple model: loss of each totally disrupted cell adhesion, and thus completely halted morphogenesis (Cox *et al.*, 1996; Müller and Wieschaus, 1996; Tepass *et al.*, 1996; Sarpal *et al.*, 2012). Loss of the polarity regulator Baz/Par3 had similar effects (Müller and Wieschaus, 1996; Harris and Peifer, 2004). However, as the field began to assess other players, this simple picture no longer held true. In embryos lacking Cno, for example, cell adhesion is not drastically compromised. However, virtually every morphogenetic movement was disrupted, from mesoderm apical constriction to cell intercalation during germband elongation to collective cell migration during dorsal closure and head involution (Boettner *et al.*, 2003; Sawyer *et al.*, 2009, 2011). Further, Cno had mechanosensing properties, responding to elevated tension on AJs, and strengthening AJ–cytoskeletal connections (Yu and Zallen, 2020; Perez-Vale *et al.*, 2021). In Cno's absence, AJs and the cytoskeleton detach. These and other data reveal a mechanoresponsive AJ, where force leads to recruitment of multiple proteins to strengthen connections. Surprisingly, many of these proteins are individually dispensable; for example, Sidekick, Ajuba, and Vinculin mutant flies are viable and fertile (Maartens *et al.*, 2016; Razzell *et al.*, 2018; Finegan *et al.*, 2019; Rauskolb *et al.*, 2019). However, close examination revealed transient defects in AJ–cytoskeletal connections that emerge when cells change shape and move.
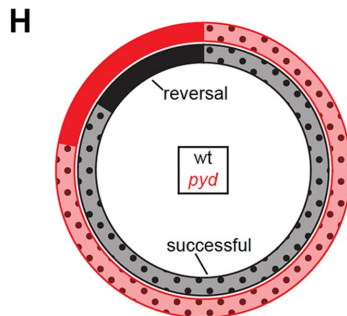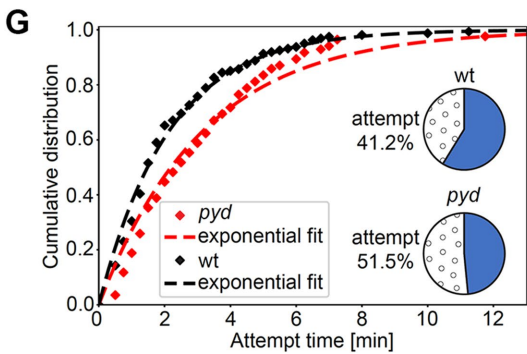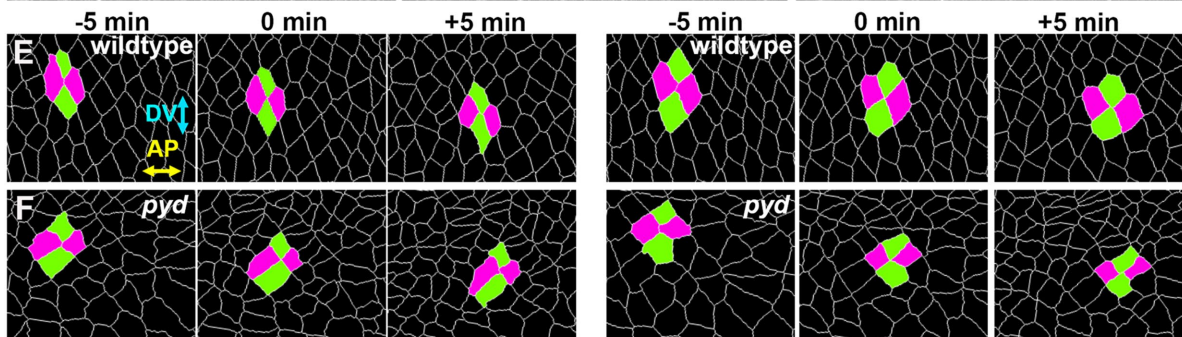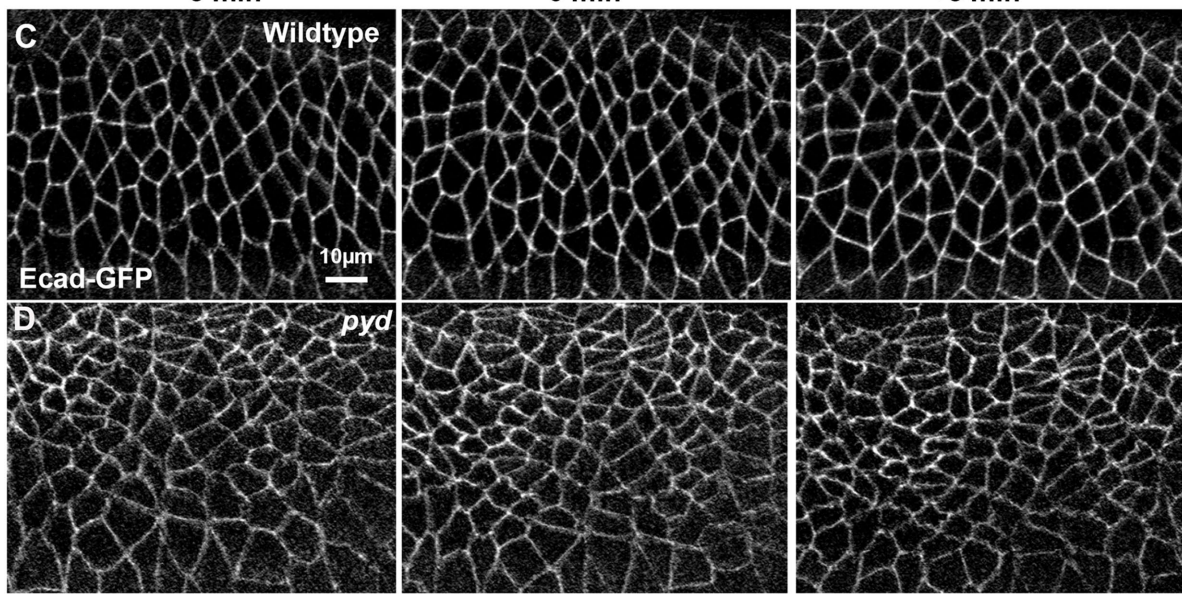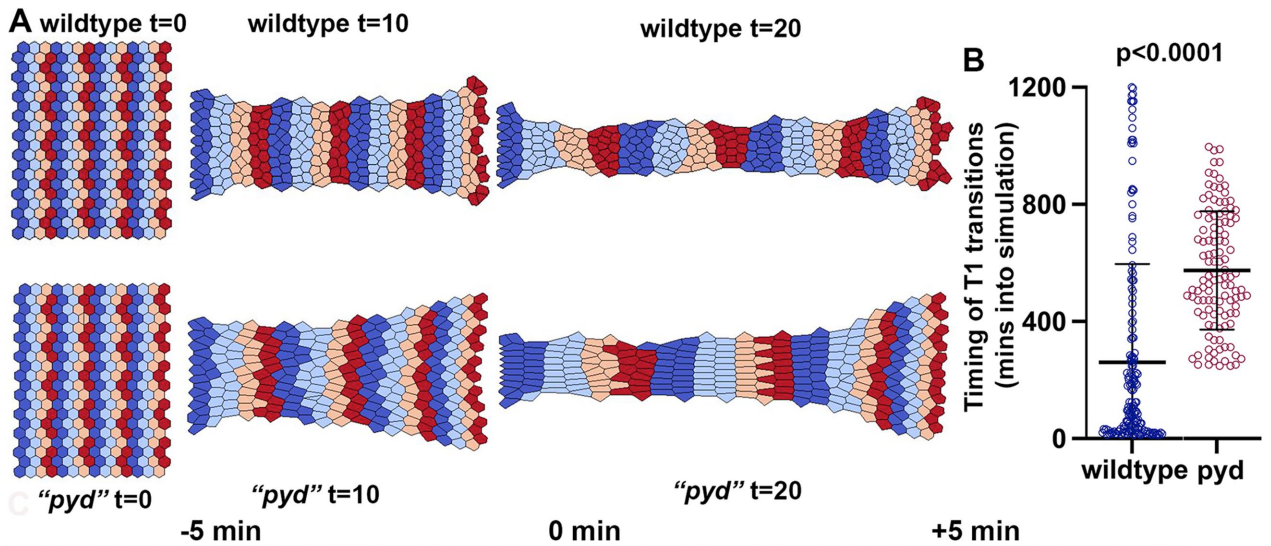
We placed Pyd into this continuum. Existing data suggested a protein whose function did not match those previously examined. Zygotic null *pyd* mutants are viable, unlike *cno*. However, many (but not all) M/Z *pyd* mutants die as embryos (Choi *et al.*, 2011), unlike embryos lacking Sidekick, Ajuba, or Vinculin. We thus directly compared Pyd function to that of Cno in early embryonic morphogenetic events. This revealed that M/Z *pyd* mutant phenotypes overlap with phenotypes of its interaction partner Cno, but that Pyd plays a less essential role. For example, while many M/Z *pyd* mutants have defects in mesoderm invagination, these are often subtle, with the failure to close restricted to the anterior or posterior ends of the mesoderm. Similarly, while we observe apical gaps in AJs under elevated tension—TCJs and aligned AP borders—these are much less frequent than those seen after complete Cno loss, and given the embryonic viability of almost half the M/Z *pyd* mutants, most gaps must reseal. Finally, the defects in integrity of the ventral epidermis seen after Cno loss are not seen in M/Z *pyd* mutants. Thus, while both Cno and Pyd contribute to making AJ–cytoskeletal connections robust, their relative importance differs.

One of the most striking phenotypes we observed in M/Z *pyd* mutants was alteration in cell shape. In mutants, stacks of cells elongated along the AP axis accumulated during germband elongation.

Similar phenotypes were observed in *sdk* mutants (Finegan *et al.*, 2019), where, as the invaginating hindgut pulls on the tissue, the germband elongates, thus elongating cells, slowed cell rearrangements prevent T1 resolution. The reduced contractility of AJs along the plane of the junction that we observed in M/Z *pyd* mutants may help explain the slowed/stalled constriction of AP borders; *sdk* mutants also have reduced junctional tension (Letizia *et al.*, 2019). Similar stacks of elongated cells are also seen in *cno* mutants (Sawyer *et al.*, 2011; Perez-Vale *et al.*, 2021), but the underlying mechanisms are likely not identical, as the obvious detachment of myosin from AP AJs seen after Cno loss (Sawyer *et al.*, 2011) is not seen in M/Z *pyd* mutants. This suggestion of different mechanisms of action is consistent with our earlier observation that Cno and Pyd act in parallel in stabilizing AJs and epithelial integrity; M/Z *pyd* mutants in which Cno is also knocked down using short hairpin RNA (shRNA) have defects in AJ stability and epithelial integrity that occur earlier and are much more substantial than those seen in either mutant alone (Manning *et al.*, 2019). One way their functions diverge is that Cno is enriched on AP borders, where myosin is enriched and contractility is the highest, while Pyd is enriched with Baz and the cadherin–catenin complex on DV cell borders. However, both are enriched at TCJs, and their respective enrichments at those sites are mutually dependent. This may involve direct protein–protein interactions, which are known to occur between Cno and Pyd (Takahashi *et al.*, 1998) and between their mammalian homologues (Ooshio *et al.*, 2010). Alternately, it may be indirect; for example, the reduction in membrane tension seen after Pyd loss might affect Cno recruitment indirectly, via Cno's mechanosensitive recruitment (Yu and Zallen, 2020; Perez-Vale *et al.*, 2021).

Our new data, and the analyses of many labs that have gone before, continue to reinforce and expand the idea that the AJ is a complex, mechanoresponsive machine with many overlapping feedback loops. One example that emerged here is the role of Pyd in maintaining junctional protein planar polarity. M/Z *pyd* mutants resemble *cno* mutants in that AJ proteins and Baz are reduced at AP borders, thus substantially enhancing their planar polarity. Early work defined a reciprocal relationship between myosin and Baz— they are enriched on opposite cell borders (Bertet *et al.*, 2004; Zallen and Wieschaus, 2004), and each antagonizes the others recruitment (Blankenship *et al.*, 2006; Simoes *et al.*, 2010). Cno loss leads to myosin detachment from AP borders without altering myosin planar polarity (Sawyer *et al.*, 2011). Intriguingly, as myosin expands laterally from the AP border, Baz localization becomes more restricted to the center of the DV border, perhaps due to myosin/Baz antagonism. We thus were surprised to see that while Pyd loss

FIGURE 4: Pyd and Cno are mutually required for one another's enrichment at TCJs, and M/Z *pyd* mutants have reduced junctional tension. (A, B, D, E) Stage 7 embryos. (A) In wild type Cno is enriched at TCJs (arrows). (B) Cno TCJ enrichment is reduced in M/Z *pyd* mutants (arrows). (C) Quantification of Cno TCJ enrichment. Three embryos and thirty TCJs per genotype; significance was determined by an unpaired two-tailed *t* test. (D) In wild type Pyd is mildly enriched at TCJs (arrows). (E) *cno* RNAi reduces Pyd junctional localization and TCJ enrichment (arrows). (F) Quantification of Pyd TCJ enrichment. Three embryos and thirty TCJs per genotype; significance was determined by an unpaired two-tailed *t* test. (G, H) Still frames from movies of stage 7 embryos, expressing Ecad-GFP. Junctions were severed with a laser and junctional recoil was measured. Green line = TCJs before cutting. Purple line = TCJ position after 10 s. (I) Vertex displacement vs. time plot for junction cuts. Dashed curves represent the mean with SEM (error bars) of displacement of junction cuts from the wild-type and *pyd* mutant embryos during germband extension. Solid curves represent the one-phase association fitting of experimental data. $N = 10$ junctions from 8 wild-type embryos and 10 junctions from 7 *pyd* mutant embryos, two-way ANOVA, Sidak's multiple comparisons test; ****, $p < 0.0001$. (J) Mean with SEM of initial recoil velocities from the one-phase association fitting in I. Unpaired two-sided *t* test; ***, $p < 0.001$. (K) Mean with SEM of K values from the one-phase association fitting in I, which indicate the ratio between the elasticity of the junction and the viscosity coefficient. Unpaired two-sided *t* test; ns, not significant.

A wildtype t=0   wildtype t=10   wildtype t=20

B p<0.0001

C *"pyd"* t=0   *"pyd"* t=10   *"pyd"* t=20

C Wildtype -5 min / 0 min / +5 min
Ecad-GFP   10μm

D *pyd*

E wildtype -5 min / 0 min / +5 min   wildtype -5 min / 0 min / +5 min
DV / AP

F *pyd*   *pyd*

G

H reversal   wt / *pyd* / successful

strongly elevated Baz planar polarity, it did not disrupt attachment of myosin to AP borders. Thus, altered planar polarity does not require myosin detachment, perhaps suggesting it is a more direct response to contractility.

High-resolution imaging reveals new insights into the complexity of AJ supermolecular architecture

The multiprotein network linking AJs to the cytoskeleton is characterized by proteins that each have multivalent linkages to one another (Fernandez-Gonzalez and Peifer, 2022), raising questions about whether and how they segregate at the architectural level. Scientists studying the cell–matrix junctions pioneered ideas about how a complex network of proteins might form a layered architecture (Case and Waterman, 2015). Work in cultured mammalian cells has begun to suggest a similar layered architecture for cell–cell junctions, with membrane-proximal cadherin tails segregated from the actin cytoskeleton by an interface containing Vinculin, VASP, and Zyxin (Oldenburg et al., 2015; Bertocchi et al., 2017). Electron microscopy also revealed a layered cytoskeletal architecture at bicellular borders, with an Arp2/3-generated branched actin network adjacent to the Cadherin tails, while linear, myosin-decorated actin arrays are found further into the cytoplasm (Efimova and Svitkina, 2018). We sought to extend this effort to examine AJ architecture in vivo during morphogenesis.

In envisioning AJ architecture, we must also consider the accumulating evidence that AJs have at least some attributes of phase-separated biomolecular condensates (Sun et al., 2022). These non–membrane bound multiprotein complexes assemble by multivalent interactions, some of which are mediated by intrinsically disordered regions (Harmon et al., 2017). Intrinsically disordered regions are a feature of many AJ scaffolding proteins, including Cno/Afadin and Pyd/ZO-1. ZO-1, Pyd's vertebrate homologue, can phase separate both in vitro and in vivo (Beutel et al., 2019; Schwayer et al., 2019). ZO-1 droplets can form in the cytoplasm, and as junctions form in cultured cells and zebrafish embryos, they dock on the membrane and then spread. Phase separation of ZO-1 is needed for tight junction formation in 3D cultured cells, and for mechanosensitivity and epithelial tissue spreading during zebrafish gastrulation (Beutel et al., 2019; Schwayer et al., 2019). Multiple other AJ proteins are also reported to phase separate, including the Baz homologue Par3 (Liu et al., 2020) and the Arm homologue β-catenin (Zamudio et al., 2019).

In *Drosophila*, AJs assemble during cellularization, as Baz organizes smaller cadherin–catenin complex and Baz puncta into apical spot AJs, with three to five SAJs per ~5-µm bicellular border (McGill

et al., 2009). Each SAJ is roughly 0.5 µm in the *XY* and 2.5 µm in the *XZ*, and contains ~1500 cadherin–catenin complexes and ~225 Baz proteins (McGill et al., 2009). Our data reveal that during germband extension, AJ architecture evolves. At stage 8 we observed 20–50 Arm puncta per 10 µm of BCJ, thus puncta number per unit membrane increases two- to fivefold, while the average puncta width in the *XY* was reduced to 0.24 µm.

During cellularization Cno localizes with AJ proteins in SAJs, but is more enriched at TCJs--Cno is 5-fold enriched there relative to bicellular SAJs, and at TCJs Cno extends ~2µm deeper along the apical-basal plane (Bonello et al., 2018). Here we used high-resolution imaging to examine how the relationship between Cno and the core AJ complex evolves during germband extension. We initially imagined two possibilities: co-localization of Arm and Cno in puncta, or layered architecture, with Cno surrounding Arm. Instead, we got a surprise--while Arm and Cno overlap in many puncta, we observed clear differential localization of these junctional proteins. Their relative enrichment in individual puncta can vary substantially. This was also true for Arm and Baz. In this case the more apical enrichment of Baz relative to Arm was accompanied by differential enrichment in puncta. Our data also suggest that Cno and Baz may extend somewhat more membrane distal than Arm, consistent with Arm's localization to the membrane-found Ecad tail, while Cno and Baz likely interact in a more multivalent way with multiple junctional and cytoskeletal proteins.

Perhaps the biggest surprise from our imaging was the localization of Pyd. Phase separating ZO-1 can recruit other junctional proteins in vitro (Beutel et al., 2019). However, in vivo the localization of Pyd we observed was quite different from that of the other AJ proteins we examined. Rather than localizing to membrane-proximal puncta, Pyd localized to strands that overlapped the junctional puncta but could extend much further into the cytoplasm--we observed this with both SIM and Airyscan imaging. Quantification of the breadth of the signal confirmed that Pyd localization to AJs was much broader than Arm, Cno, or Baz. One thing that we will ultimately need to consider when interpreting these data is the position of the antigen being visualized and the overall structure of the protein. Pyd, Cno, and Baz all contain long intrinsically disordered regions. If these are fully extended, they could span a considerable distance. Intriguingly, myosin and actin also extend further from the membrane than the core junctional proteins. Together, these data provide a more complex view of AJs during *Drosophila* germband extension. In one sense AJs are layered, with zones containing different proteins extending different distances from the plasma

---

FIGURE 5: Modeling suggests reducing contractility can mimic *pyd* phenotypes, while experiments reveal that T1 transitions in *pyd* M/Z embryos are slowed and reverse more often. (A) Stills from three time points in the vertex model simulations of wild-type germband extension (top) and germband extension with reduced contractility, to model *pyd* mutants (bottom). Distinct colors correspond to cells in different parasegments. (B) Quantification of the timing of T1 transitions during the simulations (172 T1 transitions for wild type and 116 transitions for the *pyd* mutant). Significance was determined by Welch's *t* test. (C, D) Stills of movies from wild type (C) and *pyd* M/Z (D) embryos expressing E-Cadherin GFP. Four movies were analyzed for each genotype. (E, F) Examples of T1 transitions of wild-type (E) and *pyd* (F) embryos are displayed. The old neighbors are marked in magenta while new neighbors are in green. Two successful T1 transitions are shown for wild type (green frames) while for *pyd* mutants one successful (green frame) and one unsuccessful (red frame) transition are displayed. (G) The cumulative distribution of attempted T1s in wild-type (black) and *pyd* mutant (red) embryos was plotted against time. The segmented lines display exponentially fitted curves to extract half times, indicating that *pyd* mutant embryos needed more time to finish a T1 attempt. The pie graphs display the percentage of direct (blue) and attempted (circles) T1s in wild-type and *pyd* mutant embryos. (H) In wild type, 84% of T1 transitions elongate the newly formed border in AP (horizontal) direction, while 16% fail and reverse after formation of a 4x vertex in wild type (black doughnut; *n* = 327 transitions). The fraction of reversed T1 transitions was elevated to 22% in *pyd* mutants (red doughnut; *n* = 216 transitions). For the analysis in G and H four movies were analyzed for each genotype.
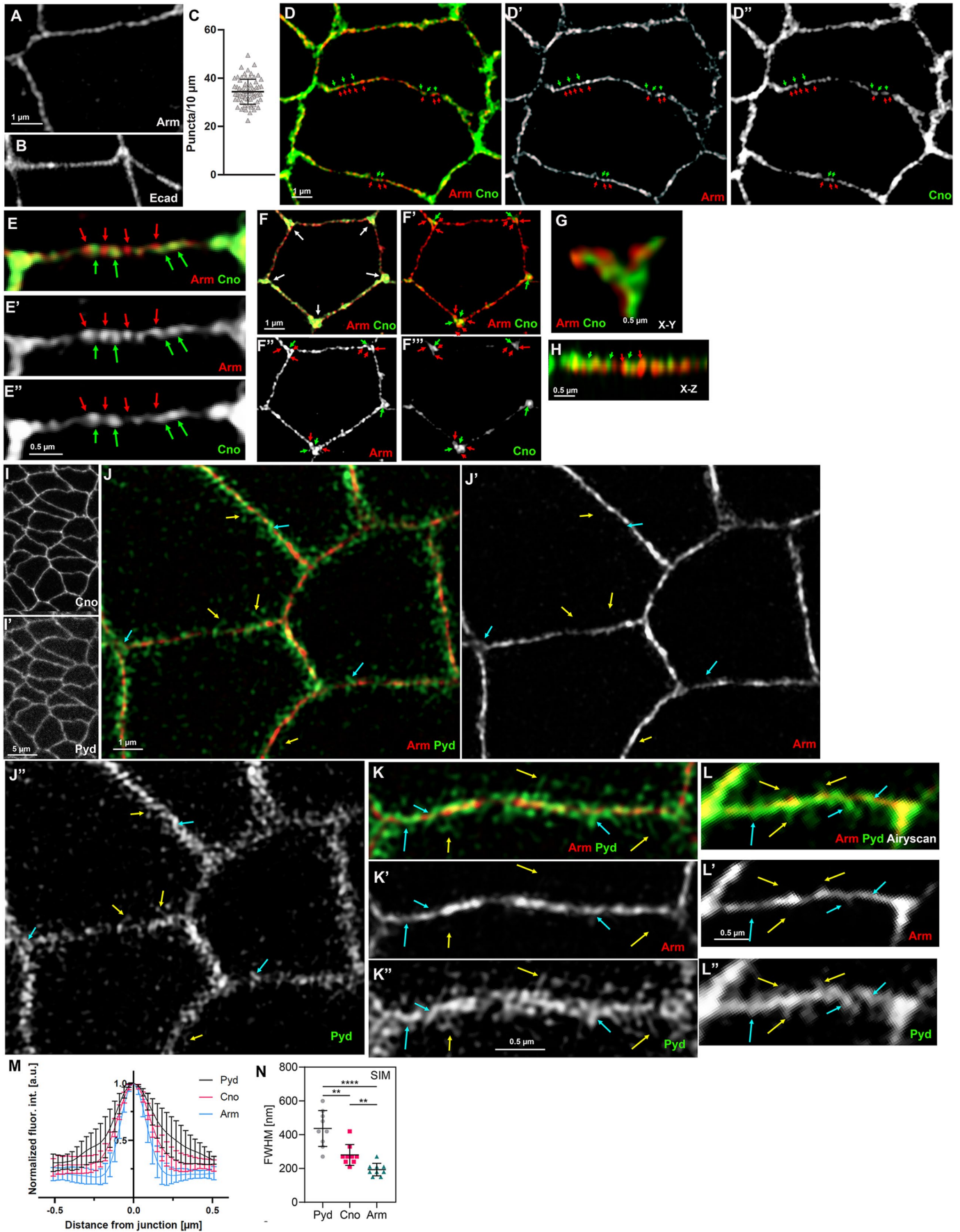
membrane. However, things are more complex. First, Pyd, actin, and myosin extend across the different zones, with Pyd localizing to discrete strands. Second, even within a "layer," Arm and Cno are differentially enriched in different puncta. Does this imply partial segregation by affinity, with Cno more avidly associating with Cno than with Arm, and vice versa? Future work will be needed to begin to sort out these issues. Together, these data suggest that rather than a single mechanosensitive multiprotein complex at AJs, it is possible there are multiple subcomplexes assembled by multivalent connections.

What do these data suggest about Pyd's mechanism of action?

With our new insights into Pyd localization and the effects of its loss, what might it imply about Pyd's mechanism of action? We can rule out some simple models. Phase separating ZO-1 can recruit other junctional proteins in vitro, including Afadin (Beutel *et al.*, 2019). However, Pyd localization is strikingly different from that of Cno, Baz, or Arm. Further, we did not observe obvious mislocalization of Arm, Cno, or Baz in M/Z *pyd* mutants. All continued to differentially localize to membrane-proximal puncta, though Baz distribution may have been slightly broadened. This suggests that Pyd is not responsible for the junctional localization of those proteins, or for junctional substructure of the more membrane-proximal "layers." Consistent with this, Pyd did not alter Ecad mobility as assessed by FRAP. Our data also suggest that, unlike Cno, Pyd is not required for the association of myosin cables with AJs along AP cell borders. Pyd does reinforce junctions under elevated tension, but its role is less essential than that of Cno. However, Pyd loss does reduce junctional contractility.

Given this, we think several speculative models are possible. One possibility is that Cno and Pyd play similar but parallel roles, simply linking core junctional proteins and actin, with Cno's role more essential and with Cno and Pyd differentially strengthening DV versus AP borders. However, their very distinctive localization patterns suggest more substantial differences in function. The Pyd strands extending membrane distal are very intriguing. Mammalian ZO-1 can dimerize via its PDZ2 domain (Utepbergenov *et al.*, 2006; Chen *et al.*, 2008) and may also dimerize via its SH3/GUK domains

(Umeda *et al.*, 2006). ZO-1 is critical for formation of the continuous strands of tight junction proteins at mammalian tight junctions (Umeda *et al.*, 2006), a function that requires PDZ2 (Rodgers *et al.*, 2013). Perhaps Pyd/ZO-1 forms polymers, which we visualize as the strands. We did not see obvious phase-separated puncta in the cytoplasm via immunostaining, and the strands we observed are distinct from the more spherical puncta previously seen (e.g., Beutel *et al.*, 2019), but these may be present earlier in AJ assembly. It will be of interest to GFP-tag Pyd at its endogenous locus and examine its localization as AJs form and evolve.

We hypothesize that AJs connect to the actomyosin cytoskeleton in different ways at BCJs and TCJs. In this model, the connections of the cytoskeleton to cadherin–catenin clusters at BCJs may not be under the same degree of "molecular force" as those at TCJs. Consistent with this, antibodies detecting the open state of α-catenin are enriched at TCJs under tension in mammalian cells (e.g., Choi *et al.*, 2016), and proteins that can sense tension like Cno are enriched at TCJs (Yu and Zallen, 2020; Perez-Vale *et al.*, 2021). We imagine that in the germband extending embryo, AJ/cytoskeletal connections are under somewhat elevated tension at AP borders, where contracting myosin cables connect side on to AJs, but that these connections are under even more tension at TCJs, where we envision cables anchor end on to AJs. In M/Z *cno* mutants, myosin detaches and apical junctional gaps arise at both sites (Sawyer *et al.*, 2011), suggesting reduced fidelity of both sorts of AJ–cytoskeletal connections. One intriguing aspect of the myosin detachment we previously observed in *cno* mutants is that spot connections to AJs remain, pulled out in strands (Sawyer *et al.*, 2011). Perhaps this reflects a role of Cno in lateral cross-linking of cadherin–catenin complexes, allowing them to jointly resist force perpendicular to the membrane. The lack of myosin detachment at AP borders in *pyd* mutants may suggest Pyd does not share this function. Another puzzling issue is why apical AJ gaps appear at aligned AP borders in both mutant genotypes, if force is primarily directed parallel to the membrane in these locations.

We also must define the mechanism by which Pyd maintains tension at AJs. The similar reduction of junctional tension in *sdk* mutants may provide a clue (Letizia *et al.*, 2019). Sdk is strongly enriched at TCJs (Finegan *et al.*, 2019; Letizia *et al.*, 2019), suggesting

FIGURE 6: The cadherin–catenin complex and Cno are differentially enriched in junctional puncta along bicellular borders and at TCJs, while Pyd localizes to strands that span a broader region than the core junctional proteins. (A, D–H) SIM imaging, stage 7–8 embryos. (A) Arm localizes to small puncta along bicellular borders. (B) Similar puncta are seen when visualizing Ecad-GFP using the Airyscan module. (C) Quantification of Arm puncta per 10 μm; 10 borders were analyzed in each of four different embryos. (D, E) Cno is enriched at AP borders and TCJs. Cno and Arm both localize to puncta along bicellular borders, but some puncta are more enriched for Arm (red arrows) and others are more enriched for Cno (green arrows). (F) Cno is strongly enriched at TCJs (F, white arrows). When the Cno signal is artificially reduced (F'), it reveals that Arm and Cno (red vs. green arrows) are enriched in different puncta at TCJs. (G, H) Images of representative TCJ and BCJ 3D rendered in Imaris. G is in *X-Y* plane and H is in the *X-Z* plane. (G) Differential localization of Arm and Cno at a TCJ, viewed in the *X-Y* plane. (H) Differential localization of Arm and Cno at a bicellular border, viewed in the *X-Z* plane. (I) Standard confocal imaging. Pyd signal appears less tightly localized to junctions than Cno. (J, K) SIM imaging, stage 8 embryos. While Arm localizes tightly to puncta along the plasma membranes, Pyd localization extends more broadly. Pyd localizes to strands that align along or perpendicular to the AJs (cyan arrows), and also can be seen localized to finer strands that project into the cytoplasm (yellow arrows). (L) Airyscan imaging. While images are less sharp, Pyd localization is also revealed to be much broader than that of Arm. (M) Breadth of signal of Arm, Cno, and Pyd, assessed perpendicular to the plasma membranes. For all proteins and genotypes a total of nine junctions in three embryos were measured. Error bars represent SD and the significance was determined by an unpaired two-tailed *t* test. (N) Measurements of the full width of fluorescence intensities measured across junctions at half of the normalized intensity maximum (FWHM) in wild-type embryos imaged with SIM. Pyd (gray) was stained with Alexa-568, Cno (red) with Alexa-647, and Arm (blue) with Alexa-488. Mean is the broad line, and the significance was quantified with unpaired, two-tailed *t* tests. *p* values are **, ≤0.01; ***, ≤0.001; ****, ≤0.0001.
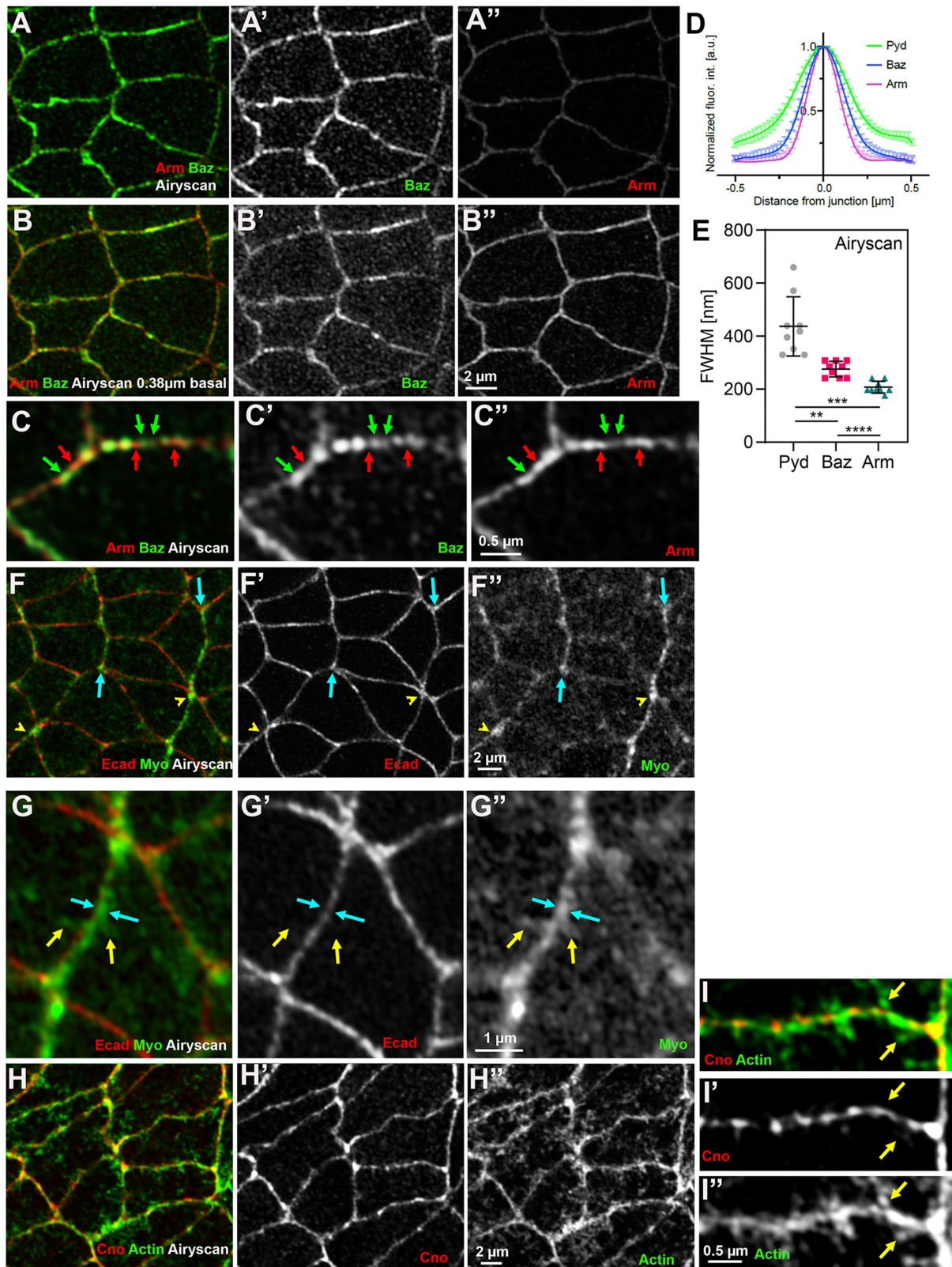
FIGURE 7: Baz and Arm are differentially enriched in junctional puncta, while Myosin occupies a broader zone along bicellular junctions than core AJ proteins. (A–C, F–I) Stages 7 and 8, Airyscan imaging. (A, B) Arm and Baz in Z sections 0.39 μm apart. Baz is stronger in the more apical section, while Arm is stronger in the more basal section. (C) Arm and Baz overlap but are differentially enriched in puncta along bicellular borders. Some puncta are enriched for Arm (red arrows) and some for Baz (green arrows). (D) Breadth of signal of Arm, Baz, and Pyd, assessed perpendicular to the plasma membranes. For all proteins and genotypes a total of nine junctions in three embryos were measured. Error bars represent SD; the significance was determined by an unpaired two-tailed t test. (E) Measurements of the full width of
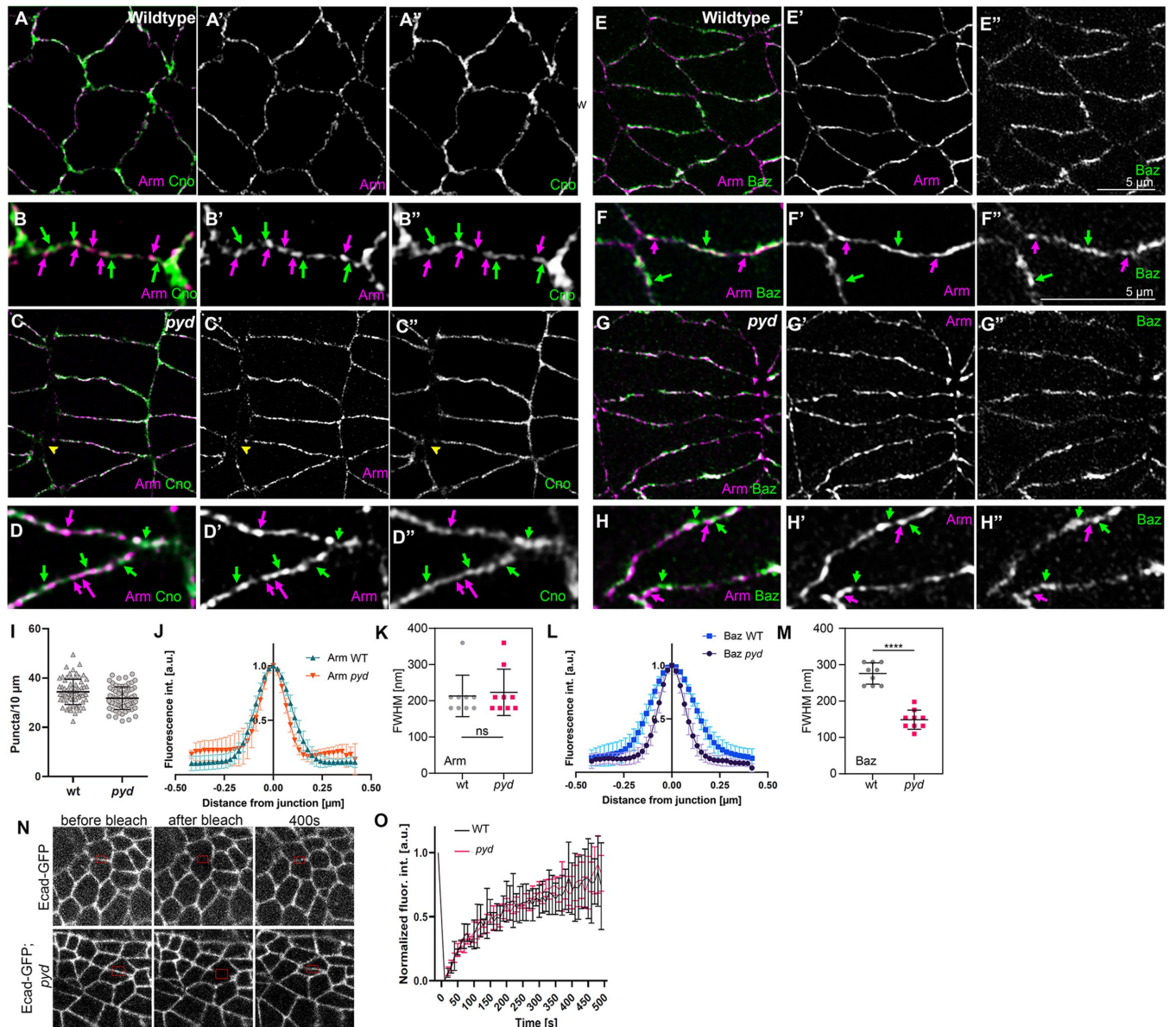
FIGURE 8: Using SIM imaging to explore the role of Pyd in AJ molecular architecture. (A–H) SIM imaging, stage 7–8 embryos. (A–D) In both wild type and M/Z *pyd* mutants. Arm and Cno continue to differentially localize to puncta along bicellular borders. (E–H) In both wild type and M/Z *pyd* mutants Arm and Baz continue to differentially localize to puncta along bicellular borders. (I) Arm puncta number per 10 μm of bicellular border does not substantially change in M/Z *pyd* mutants relative to wild type. (J, K) Arm puncta distribution perpendicular to the membrane is not altered in M/Z *pyd* mutants. (K) For measurements of Arm FWHM in wild-type (gray) and *pyd* embryos (red) SIM was used and Arm was stained with Alexa-488 in wild-type and Alexa-647 in *pyd* embryos. (L, M) Baz puncta distribution perpendicular to the membrane appears slightly broadened in M/Z *pyd* mutants. (M) For measurements of Baz FWHM in wild-type (gray) and *pyd* embryos (red) Airyscan was used and Baz was stained with Alexa-647 in wild-type and Alexa-488 in *pyd* embryos. Nine junctions in a total of three embryos were measured. The broad lines indicate the mean, and the significance was quantified with unpaired, two-tailed *t* tests. *p* values are **, ≤0.01; ***, ≤0.001; ****, ≤0.0001. (N, O) FRAP of junctional Ecad-GFP in wild type and M/Z *pyd* mutants. Six wild-type junctions in four embryos and seven *pyd* junctions in three embryos were quantified. Error bars represent SD.

fluorescence intensities measured across junctions at half of the normalized intensity maximum (FWHM) in wild-type embryos imaged with Airyscan. Pyd (gray) was stained with Alexa-568, Baz (red) with Alexa-647, and Arm (blue) with Alexa-488. Mean is the broad line, and the significance was quantified with unpaired, two-tailed *t* tests. *p* values are **, ≤0.01; ***, ≤0.001; ****, ≤0.0001. (F, G) Embryo expressing Ecad-GFP and mCh-Myosin. Myosin is enriched at AP borders (F, arrows) and rosette centers (F, arrowheads). Myosin localization at these borders is broader than that of Arm (G, cyan arrows) and strands extend membrane distal (G, yellow arrows). (H, I) Actin localization at cell junctions is broader than that of Cno. In I arrows indicate actin structures extending membrane distal.

Parameter	Description	Value	Reference(s)
η	Drag coefficient	1.0	Kursawe *et al.*, 2017
T	Simulation end time	300	–
Δt	Timestep	0.001	Kursawe *et al.*, 2017
d_{min}	T1 swap threshold	0.01	Kursawe *et al.*, 2017
p	T1 swap distance multiplier	1.5	Kursawe *et al.*, 2017
K	Elastic coefficient	1	Farhadifar *et al.*, 2007
A_0	Cell target area	1	Farhadifar *et al.*, 2007
Γ	Contractility coefficient	0.04	Farhadifar *et al.*, 2007
Λ_{int}	Internal line-tension coefficient	0.05	Tetley *et al.*, 2016,
Λ_{bdy}	Boundary line-tension coefficient	$2\Lambda_{int}$	Tetley *et al.*, 2016
Λ_{sup}	Mismatched boundary line-tension coefficient	$8\Lambda_{int}$	Tetley *et al.*, 2016

TABLE 1: The parameters and their values used in our vertex model simulations.

it acts there. Perhaps both Sdk and Pyd ensure the stability of the hypothesized "end-on" connections of actomyosin cables at TCJs. This role is similar to the role we have suggested Cno plays during dorsal closure, when the leading-edge actin cable is anchored cell–cell at specialized leading-edge AJs (Manning *et al.*, 2019). The localization of the barbed end actin polymerase Ena to TCJs at both stages (Gates *et al.*, 2007; Manning *et al.*, 2019), and strong genetic interactions between *cno*, *pyd*, and *ena* (Choi *et al.*, 2011) may suggest a special role for anchoring and maintaining actin barbed ends at TCJs. One important experiment remaining is to test whether Cno loss also reduces junctional tension. This is just one of many new questions raised by this work, as the field continues to unravel the complex, multivalent interactions that ensure robust AJ–cytoskeletal connections as cells change shape and move.

MATERIAL AND METHODS
Request a protocol through *Bio-protocol*.

Fly stocks and handling
All crosses and embryo collections were done at 25°C if not mentioned otherwise. *cno RNAi* embryo collections were kept at 29°C. *y w* was used as our wild-type control. M/Z *pyd* mutant embryos were collected by crossing homozygous mutant virgin females with heterozygous males, as homozygous males are basically sterile. To distinguish M/Z mutant embryos from zygotically rescued ones, the embryos were stained with an antibody directed against Pyd. For live imaging, stocks that were balanced over a TM3 with a GFP-reporter were used. Stocks used are found in Table 2.

Fixation and immunohistochemistry
Embryos were collected in plastic cups on apple juice agar plates at 25°C. The embryos were either fixed by formaldehyde treatment or

by heat fixation, depending on the staining. For heat fixation, the chorion was removed by treatment with 50% sodium hypochlorite for 5 min following three washing steps with wash buffer (68 mM NaCl, 0.03% Triton). The embryos were then transferred into pre-boiled salt buffer (68 mM NaCl, 0.03% Triton, 8 mM EGTA) and cooled down after 10 s with prechilled salt buffer. After the solution cooled down, the embryos were transferred into a 50% heptane, 50% MeOH/EGTA (95% MeOH, 5% EGTA) solution and the vitelline membrane was popped by vigorous shaking, followed by three washing steps in MeOH/EGTA. The embryos were stored at –20°C in MeOH/EGTA. For formaldehyde fixation, the embryos were collected as above, and after removing the chorion, the embryos were fixed in a 1:1 mixture of heptane and formaldehyde (4% in phosphate-buffered saline [PBS], 8 mM EGTA) for 20 min followed by removal of the vitelline membrane as above. For phalloidin staining and myosin imaging, fixation was done in 1:1 heptane: 8% formaldehyde in PBS, 8 mM EGTA and the vitelline membrane was removed manually. Antibodies used are in Table 3.

Image acquisition
Imaging of fixed samples was performed on the following Zeiss (Oberkochen, Germany) laser scanning confocal microscopes: LSM-5 Pascal with a 40× EC Plan-Neofluar objective (oil, 1.3 NA) or LSM 880 with a 40× Plan-Apochromat objective (oil, 1.3 NA) and 63× Plan-Apochromat objective (oil, 1.4 NA). All fixed and stained embryos were mounted in Aquapolymount or Prolong Diamond mounting media on No. 1.5 cover slides. Airyscan imaging was done with the Zeiss LSM 880 and Airyscan module with the aforementioned 63× Plan-Aprochromat objective. The pixel size was set to half the size of the theoretical optical resolution resulting in 42.6 nm/pixel and the step size in Z was set to half of the axial resolution resulting in 200 nm. Airyscan processing was done with the

Stock	Reference
pyd[B12]	Bloomington #94725
ubiquitin-E-Cadherin GFP, Sqh-mCherry	J. Zallen (Sloan-Kettering, NY)
E-Cadherin GFP	Bloomington #60584; Huang *et al.*, 2009
cnoRNAiV20	Bloomington #33367
Mat-tub-Gal4;Mat-tub-Gal4	Bloomington #80361

TABLE 2: Fly stocks.

Antibodies/probes	Species	Dilution	Source
Anti-Arm (N2 7A1)	Mouse 2a	1:100	Developmental Studies Hybridoma Bank (DSHB)
Anti-Baz	Rabbit	1:1000	J. Zallen (Memorial Sloan-Kettering Cancer Center)
Anti-Cno	Rabbit	1:1000	Sawyer *et al.*, 2009
Anti-Pyd (PYD2)	Mouse 2b	1:1000	DSHB
Secondary antibodies			
Alexa Fluor-488, 568, and 647		1:500	Life Technologies
Other probes			
Phalloidin-Alexa 488		1:1000	Life Technologies

TABLE 3: Antibodies and probes used.

automatic settings in ZEN black (Zeiss). SIM imaging was performed on a Nikon N-SIM using a 100× SR APO TIRF objective (oil, 1.49 NA) with a lateral pixel size of 31.8 nm and a step size in *Z* of 100 nm. Image reconstruction was done with NIS Elements AR version 4.51 (Nikon).

Laser ablation and quantification

Laser ablation was conducted as previously described (Lv *et al.*, 2022). Briefly, stage 7 embryos from wild-type or *pyd* mutant flies expressing Ecad-GFP were collected for junction ablation. Dechorionated embryos were aligned on an agar block and transferred to a cover slide with heptane glue and dried in a desiccation chamber for 2 min, and then covered with halocarbon oil. The UV laser (DPSL355/14, 355 nm, 70 µJ/pulse; Rapp Optoelectronic) was introduced from the epi-port of the confocal microscope (Zeiss LSM 980). Junction ablation was performed with 5% laser power and 50 ms exposure time during the recording mode (100× oil, NA 1.4). The displacement of vertex (*L*(*t*)) of ablated junctions was measured manually in Fiji/ImageJ. The displacement was fitting as a Kelvin-Voigt fiber model (Fernandez-Gonzalez *et al.*, 2009) to the following equations on Prism8 (Liang *et al.*, 2016).

Extraction of initial recoil values:

$$\varepsilon(t) = L(t) - L(0) = F_0/E \cdot \left(1 - e^{\left(-\left[^{(E/\mu)^*t}\right]\right)}\right) \qquad (1)$$

where F_0 is the tensile force present at the junction before ablation, E is the elasticity of the junction, and μ is the viscosity coefficient related to the viscous drag of the cell cytoplasm. As fitting parameters for the above equation initial recoil = $d\varepsilon(0)/dt = F_0/\mu$ (Eq. 2) and K values = E/μ (Eq. 3) were introduced.

Live imaging

For live imaging, the embryos were collected from agarose plates and dechorionated in 50% bleach for 90 s and then aligned on a piece of agarose gel and glued to a No. 1.5 cover slide with heptane glue. The embryos were covered with halocarbon oil and either covered by a dish spanned with an oxygen-permeable foil or the coverslip was glued to a metal holder with double-sided tape.

Live imaging for the analysis of T1 transitions was performed on a Zeiss LSM 980 with Airyscan 2 in multiplex CO-8Y mode with a 63× Plan-Apochromat Oil DIC M27 objective (1.4 NA). The frame size was set to 1564 × 1364 pixels with a lateral pixel size of 85 nm, a step size in z of 0.5 µm, and a frame time of 105.06 ms. We imaged z stacks in an interval of 15 s, using the multiplex CO-8Y mode with the Airyscan 2 detector.

FRAP was done on a ZEISS LSM 880 and a 63× oil objective as described above. Z stacks with a step size of 0.5 µmwere recorded in an interval of 10 s. The frame size was set to 196 × 196 pixels with a lateral pixel size of 90 nm, an axial step size of 0.5 µm, and a frame time of 121.20 ms. For bleaching, the 488-nm laser was set to 100% laser power with 70 iterations.

Image analysis and quantification

FRAP of Ecad was done in embryos expressing Ecad-GFP in wild-type or *pyd* mutant backgrounds. The analysis was done in Fiji/ImageJ by measuring the mean fluorescence intensity of the bleached region. The axial and lateral movement of the bleached region was corrected manually. To correct for bleaching during imaging, the fluorescence intensity of a junction outside of the bleached region was also measured. Six wild-type junctions in four embryos and seven *pyd* junctions in three embryos were quantified, normalized to the junction outside the bleached region and then normalized to Min and Max to adjust for differences in bleaching before they were averaged. The error bars represent the SD.

For the quantification of the width of Baz, Arm, Cno, and Pyd signal across the junctions, the mean fluorescence intensity of a 10-pixel-thick line that was drawn across the junctions was measured in Fiji ImageJ. For all proteins and genotypes a total of nine junctions in three embryos were measured. The individual measurements were then normalized to their maximum, which also represented the center on the *y* axis in the plots. All measurements were averaged, and the error bars represent the SD. To determine the significance of junction signal breadth, we measured the full width of the normalized fluorescence intensity of each measurement at half of the maximum intensity (FWHM). The analysis was done in Microsoft Excel by measuring the distance between negative and positive *x*-axis data points whose fluorescence intensity was closest to 0.5. In those experiments, embryos for SIM imaging were stained with the following secondary antibodies: Arm, Alexa-488; Pyd, Alexa-568; Cno, Alexa 647. For embryos in Airyscan, the following secondary antibodies were used: Cno, Alexa-488; Pyd, Alexa-568; Baz, Alexa-467.

For measurement of cell eccentricity, the ventrolateral regions of fixed embryos stained with an AJ marker were imaged by confocal microscopy and images were processed manually using Fiji/ImageJ (Schindelin *et al.*, 2012) to generate images suitable for automated segmentation. These images were aligned such that the AP axes were oriented left to right. Images were then processed by a custom MATLAB script (https://github.com/tmfinegan/Shape-analysis) to automatically segment cells, and the shape characteristics were extracted using the "regionprops" functionality. Eccentricity is a

measure of the ratio of the distance between the foci of an ellipse of best fit and its major axis length. The value is between 0 and 1. An ellipse with eccentricity 0 is a circle, while an ellipse with eccentricity 1 is a line segment.

Planar polarity of Baz, Cno, and Arm were quantified by line measurements of the mean fluorescence intensity of 20 DV, and 20 AP borders in five embryos per genotype was measured. For that, a maximum intensity projection of two to four slices that covered the apical zonula adherens was made in Fiji/ImageJ. The line width for the measurements was set to 3 pixels. To correct for background fluorescence or cytoplasmic signal, the mean fluorescence inside 20 cells was measured and subtracted from the border signal. The DV/AP ratios of all embryos were blotted in the graph as well as the average, and the error bars represent the SD.

The enrichment of Cno and Pyd at TCJs was quantified in three embryos in a total 30 TCJs per genotype by measuring the mean fluorescence intensity at tricellular junctions and three of their surrounding borders. The thickness of the line was set to 3 pixels. Each intensity value of TCJ was then divided by the average of the three neighboring BCJ values. All values were plotted in the graphs and the error bars represent the standard deviations.

For the analysis of apical gaps, they were counted in representative regions of interest (ROIs) of 14 embryos per genotype in stages 7 and 8. Each ROI measured 133×133 µm. To qualify as a gap, the distance between borders at tricellular or multicellular junctions had to exceed 1 µm; for long gaps that were aligned at AP borders one gap was counted per four cells, which corresponds roughly to the number of cells that would make up a rosette. All data points are plotted in the graph with mean and SD.

To count the number of Arm puncta along borders, the spot function in Imaris was used. For automatic detection, the estimated diameter was set to 0.1 µm and the PSF elongation along the z axis was set to 0.3 µm, background subtraction was done automatically, and the quality was set above automatic threshold, which was afterwards corrected by eye.

Images were processed in Fiji/ImageJ and Adobe Photoshop. 3D images were rendered in Imaris (Oxford Instruments).

Analysis of T1 transitions in the simulation and in vivo

In analyzing the simulations, T1 transitions were identified manually by determining when two cells that were not previously contacting shared a junction. For the segmentation of germband tissue, the 3D data was reduced to 2D by summarizing the fluorescence intensities in ZEN black. We used a custom-designed image segmentation pipeline to segment the tissue. Its core element is the machine learning–based skeletonizing of the tissue, using cycle-consistent generative adversarial networks (CycleGAN; Häring et al., 2018). The predicted segmentation was then manually corrected, using the Tissue Analyzer plugin in Fiji/ImageJ (Aigouy et al., 2016). Afterward, the data was parsed via TissueMiner (Etournay et al., 2016), and analyzed with custom written software in Python.

The detection of T1 transition was achieved by assignment of neighbor exchanges, which were defined by loss of contact of two cells with gaining new cell contacts to cells that were previously neighboring the initial cell pair. To be included in the quantification, we required a successful tracking over four frames as well as a successful T1 event was defined by maintenance of the newly established junction for at least four frames and the new junction had to obtain a minimal threshold length of 1 µm. The cell quadruplet must be stable and retain its neighbor connections for at least 10 frames. Furthermore, the area of the cells within the quadruplet was not allowed to change more than 20%.

T1 orientation. The orientation of a T1 transition is obtained by computing a *nematic director* (Etournay et al., 2016) from the midpoints of the participating cells. The orientation takes values in $(-\pi/2, \pi/2)$, which is the angle with respect to the experimentally determined anterior–posterior axis of the tissue.

4x points. The 4x points are the events where two cells of the T1 quadruplet are losing contact. If the new junction is immediately established, we speak of a direct T1 transition. The 4x point is called metastable if it takes time to resolve into establishing a new junction. The last 4x point is the one right before successful junction establishment.

Rate of T1 resolution. The T1 resolution rate is determined by fitting an exponential distribution to the cumulative distribution function of T1 attempt duration. The rate of the exponential, which equals the inverse of the mean, is called the rate of T1 resolution. Intuitively, it quantifies how long the resolution of a T1 transition will take on average. Smaller rates correspond to a longer expected attempt duration.

Confidence intervals. If not stated otherwise, error regions have been determined by calculating 95% bias-corrected and accelerated bootstrap confidence intervals with 5000 samples.

Statistical tests. If not stated otherwise, the p values for estimators have been calculated from one- or two-sided t tests. The p values to compare distributions were calculated using Kolmogorov-Smirnov tests.

Vertex model of axis extension in wild type and *pyd* mutant

We used mathematical modeling to investigate the topological implications of actomyosin contractility during *Drosophila* axis extension in a *pyd* mutant, modifying a vertex model of wild-type behavior (Tetley et al., 2016). Vertex models describe epithelial mechanics by considering the polygonal tessellation that cells' AJs form in two dimensions (Fletcher et al., 2014). In such models, the movement of junctional vertices and the intercalation of cells are governed by the strength of cell–cell adhesion, the contractility of the actomyosin cortex, and cell elasticity. We describe the epithelial sheet by a set of connected vertices in two dimensions. Assuming that the motion of these vertices is overdamped, the position $r_i(t)$ of vertex i evolves according to the first-order equation of motion

$$\eta \frac{dr_i(t)}{dt} = F_i(t) \tag{2}$$

where $F_i(t)$ denotes the total force acting on vertex i at time t and η denotes the common drag coefficient. We specify the forces acting on vertices through a "free energy" function U, for which

$$F_i = -\frac{\partial U}{\partial r_i} \tag{3}$$

Our choice of U is given by (Farhadifar et al., 2007)

$$U = \sum_\alpha \frac{K}{2}(A_\alpha - A_0)^2 + \sum_\alpha \frac{\Gamma}{2}P_\alpha^2 + \sum_{(i,j)} \Lambda_{ij} l_{ij} \tag{4}$$

The first term in this free energy function describes an area elasticity with common elastic coefficient K, for which A_α is the area of cell α and A_0 is a common "target" area, and the sum runs over all cells at time t. The second term describes the contractility of the cell perimeter P_α by a common coefficient Γ, with the sum again running over all cells at time t. The third term represents "line tensions" at cell–cell interfaces, where l_{ij} denotes the length of the interface shared by vertices i and j, the line-tension coefficient Λ_{ij} may take different values for different edges, and the sum runs over the set of interfaces at time t. Line tensions can be increased by reducing

cell–cell adhesion and/or increasing junctional myosin activity. The precise functional form of this line-tension term varies across our simulations.

In addition to these equations of motion for cell vertices, we must ensure that cells are always nonintersecting and allow cells to form and break bonds. This is achieved through an elementary operation called edge rearrangement (a "T1 swap"), which corresponds biologically to cell intercalation. Mathematically, such arrangements are necessary in the vertex model due to the finite forces acting on a cell's vertices arbitrarily far from equilibrium. We implement a T1 swap whenever two vertices i and j are located less than a minimum threshold distance d_{min} apart (taken to be much smaller than a typical cell diameter). In this case, the two vertices are moved orthogonally to a distance pd_{min} apart and the local topology of the cell sheet is modified such that they no longer share an edge.

We explicitly model the presence of an extrinsic pull in the posterior (horizontal; positive x) direction, representing the action of the posterior midgut. This extrinsic pull is modeled as follows. At each timestep, after moving each vertex a small amount according to its equation of motion and executing any neighbor exchanges (see below), we manually displace each vertex horizontally by an amount that scales linearly with the vertex's distance from the anterior edge (minimum x) of the tissue. This scaling is chosen so that the extrinsic pull exhibits a constant strain rate across the tissue. In addition, we "pin" the anterior edge of the tissue by preventing the anteriormost vertices to move in the x direction, though allowing them to move in dorsoventrally (vertically; y direction).

In summary, the configuration of the tissue is updated using the following algorithm. Starting from an initial configuration $r_i(0)$, we update the state of the system until time T over discrete timesteps Δt. At each timestep we implement any required T1 swaps; compute the forces F_i on each vertex from the free energy U; solve the equation of motion for each vertex over the timestep numerically, using an explicit Euler method; implement an extrinsic pull and boundary conditions, if specified; and finally update the positions of all vertices simultaneously. We implement this model in Chaste, an open-source C++ library that allows for the simulation of vertex models (Fletcher *et al.*, 2013).

We introduce four distinct "stripes" of cell identities within each parasegment (Tetley *et al.*, 2016). In our model, the line-tension coefficient Λ_{ij} takes one of three values, depending on the type of interface: 1) if the interface is shared by two cells of the same identity, or belongs to a single cell, then $\Lambda_{ij} = \Lambda_{int}$; 2) if the interface is shared by two cells whose identities (modulo 4) differ by 1, then $\Lambda_{ij} = \Lambda_{bdy}$; 3) if the interface is shared by two cells whose identities (modulo 4) differ by 2 ("mismatched boundary interface"), then we set $\Lambda_{ij} = \Lambda_{sup}$. We refer to 1)–3) as "internal," "boundary," and "mismatched boundary" interfaces, respectively. We choose $\Lambda_{int} < \Lambda_{bdy} < \Lambda_{sup}$ to reflect our assumption that boundary interfaces are more contractile than internal interfaces, and mismatched boundary interfaces are even more contractile.

We model the movement, shape change, and neighbor exchange of a small tissue that is initially comprised of 20 rows and 14 columns of hexagonal cells. Prior to the start of each scenario, we simulate the evolution of the tissue to mechanical equilibrium under the assumption that the line-tension coefficient takes the same value for every interface, $\Lambda_{ij} = \Lambda_{int}$. This avoids compounding the later dynamics by "artifacts" associated with starting the tissue away from the equilibrium cell size. The value of Λ_{int}, and all other parameters used in the scenarios described below, are provided in Table 1. We then modify the line-tension coefficients to

take different values for internal, boundary, and mismatched boundary interface, and implement an extrinsic pull on the tissue, as described above. Under these conditions we simulate the tissue for some time T.

REFERENCES
Aigouy B, Umetsu D, Eaton S (2016). Segmentation and quantitative analysis of epithelial tissues. Methods Mol Biol 1478, 227–239.

Bertet C, Sulak L, Lecuit T (2004). Myosin-dependent junction remodelling controls planar cell intercalation and axis elongation. Nature 429, 667–671.

Bertocchi C, Wang Y, Ravasio A, Hara Y, Wu Y, Sailov T, Baird MA, Davidson MW, Zaidel-Bar R, Toyama Y, et al. (2017). Nanoscale architecture of cadherin-based cell adhesions. Nat Cell Biol 19, 28–37.

Beutel O, Maraspini R, Pombo-Garcia K, Martin-Lemaitre C, Honigmann A (2019). Phase separation of zonula occludens proteins drives formation of tight junctions. Cell 179, 923–936. e911.

Blankenship JT, Backovic ST, Sanny JS, Weitz O, Zallen JA (2006). Multicellular rosette formation links planar cell polarity to tissue morphogenesis. Dev Cell 11, 459–470.

Boettner B, Harjes P, Ishimaru S, Heke M, Fan HQ, Qin Y, Van Aelst L, Gaul U (2003). The AF-6 homolog canoe acts as a Rap1 effector during dorsal closure of the Drosophila embryo. Genetics 165, 159–169.

Bonello TT, Perez-Vale KZ, Sumigray KD, Peifer M (2018). Rap1 acts via multiple mechanisms to position Canoe and adherens junctions and mediate apical-basal polarity establishment. Development 145, dev157941.

Case LB, Waterman CM (2015). Integration of actin dynamics and cell adhesion by a three-dimensional, mechanosensitive molecular clutch. Nat Cell Biol 17, 955–963.

Chen CM, Freedman JA, Bettler DR Jr, Manning SD, Giep SN, Steiner J, Ellis HM (1996). *polychaetoid* is required to restrict segregation of sensory organ precursors from proneural clusters in *Drosophila*. Mech Dev 57, 215–227.

Chen J, Pan L, Wei Z, Zhao Y, Zhang M (2008). Domain-swapped dimerization of ZO-1 PDZ2 generates specific and regulatory connexin43-binding sites. EMBO J 27, 2113–2123.

Choi W, Acharya BR, Peyret G, Fardin MA, Mege RM, Ladoux B, Yap AS, Fanning AS, Peifer M (2016). Remodeling the zonula adherens in response to tension and the role of afadin in this response. J Cell Biol 213, 243–260.

Choi W, Harris NJ, Sumigray KD, Peifer M (2013). Rap1 and Canoe/afadin are essential for establishment of apical-basal polarity in the *Drosophila* embryo. Mol Biol Cell 24, 945–963.

Choi W, Jung KC, Nelson KS, Bhat MA, Beitel GJ, Peifer M, Fanning AS (2011). The single *Drosophila* ZO-1 protein Polychaetoid regulates embryonic morphogenesis in coordination with Canoe/afadin and enabled. Mol Biol Cell 22, 2010–2030.

Cliffe A, Mieszczanek J, Bienz M (2004). Intracellular shuttling of a Drosophila APC tumour suppressor homolog. BMC Cell Biol 5, 37.

Cox RT, Kirkpatrick C, Peifer M (1996). Armadillo is required for adherens junction assembly, cell polarity, and morphogenesis during Drosophila embryogenesis. J Cell Biol 134, 133–148.

Djiane A, Shimizu H, Wilkin M, Mazleyrat S, Jennings MD, Avis J, Bray S, Baron M (2011). Su(dx) E3-Ubiquitin ligase dependent and independent

functions of Polychaetoid, the *Drosophila* ZO-1 homologue. J Cell Biol 192, 189–200.

Efimova N, Svitkina TM (2018). Branched actin networks push against each other at adherens junctions to maintain cell-cell adhesion. J Cell Biol 217, 1827–1845.

Etournay R, Merkel M, Popovic M, Brandl H, Dye NA, Aigouy B, Salbreux G, Eaton S, Julicher F (2016). TissueMiner: a multiscale analysis toolkit to quantify how cellular processes create tissue dynamics. eLife 5, 14334.

Farhadifar R, Roper JC, Aigouy B, Eaton S, Julicher F (2007). The influence of cell mechanics, cell-cell interactions, and proliferation on epithelial packing. Curr Biol 17, 2095–2104.

Fernandez-Gonzalez R, Peifer M (2022). Powering morphogenesis: multi-scale challenges at the interface of cell adhesion and the cytoskeleton. Mol Biol Cell 33, pe4.

Fernandez-Gonzalez R, Simoes SDM, Roper JC, Eaton S, Zallen JA (2009). Myosin II dynamics are regulated by tension in intercalating cells. Dev Cell 17, 736–743.

Fernandez-Gonzalez R, Zallen JA (2011). Oscillatory behaviors and hierarchical assembly of contractile structures in intercalating cells. Phys Biol 8, 045005.

Finegan TM, Hervieux N, Nestor-Bergmann A, Fletcher AG, Blanchard GB, Sanson B (2019). The tricellular vertex-specific adhesion molecule Sidekick facilitates polarised cell intercalation during *Drosophila* axis extension. PLoS Biol 17, e3000522.

Fletcher AG, Osborne JM, Maini PK, Gavaghan DJ (2013). Implementing vertex dynamics models of cell populations in biology within a consistent computational framework. Prog Biophys Mol Biol 113, 299–326.

Fletcher AG, Osterfield M, Baker RE, Shvartsman SY (2014). Vertex models of epithelial morphogenesis. Biophys J 106, 2291–2304.

Gates J, Mahaffey JP, Rogers SL, Emerson M, Rogers EM, Sottile SL, Van Vactor D, Gertler FB, Peifer M (2007). Enabled plays key roles in embryonic epithelial morphogenesis in *Drosophila*. Development 134, 2027–2039.

Greig J, Bulgakova NA (2021). Fluorescence recovery after photobleaching to study the dynamics of membrane-bound proteins in vivo using the *Drosophila* embryo. Methods Mol Biol 2179, 145–159.

Häring M, Großhans J, Wolf F, Eule S (2018). Automated segmentation of epithelial tissue using cycle-consistent generative adversarial networks. BioRxiv, 311373.

Harmon TS, Holehouse AS, Rosen MK, Pappu RV (2017). Intrinsically disordered linkers determine the interplay between phase separation and gelation in multivalent proteins. eLife 6, 30294.

Harris TJ, Peifer M (2004). Adherens junction-dependent and -independent steps in the establishment of epithelial cell polarity in *Drosophila*. J Cell Biol 167, 135–147.

Harris TJ, Peifer M (2005). The positioning and segregation of apical cues during epithelial polarity establishment in *Drosophila*. J Cell Biol 170, 813–823.

Huang J, Zhou W, Dong W, Watson AM, Hong Y (2009). From the cover: directed, efficient, and versatile modifications of the *Drosophila* genome by genomic engineering. Proc Natl Acad Sci USA 106, 8284–8289.

Ikenouchi J, Umeda K, Tsukita S, Furuse M, Tsukita S (2007). Requirement of ZO-1 for the formation of belt-like adherens junctions during epithelial cell polarization. J Cell Biol 176, 779–786.

Itoh M, Nagafuchi A, Moroi S, Tsukita S (1997). Involvement of ZO-1 in cadherin-based cell adhesion through its direct binding to alpha catenin and actin filaments. J Cell Biol 138, 181–192.

Itoh M, Nakadate K, Matsusaka T, Hunziker W, Sugimoto H (2018). Effects of the differential expression of ZO-1 and ZO-2 on podocyte structure and function. Genes Cells 23, 546–556.

Itoh M, Terada M, Sugimoto H (2021). The zonula occludens protein family regulates the hepatic barrier system in the murine liver. Biochim Biophys Acta Mol Basis Dis 1867, 165994.

Jung AC, Ribeiro C, Michaut L, Certa U, Affolter M (2006). Polychaetoid/ZO-1 is required for cell specification and rearrangement during *Drosophila* tracheal morphogenesis. Curr Biol 16, 1224–1231.

Katsuno T, Umeda K, Matsui T, Hata M, Tamura A, Itoh M, Takeuchi K, Fujimori T, Nabeshima Y, Noda T, *et al.* (2008). Deficiency of zonula occludens-1 causes embryonic lethal phenotype associated with defected yolk sac angiogenesis and apoptosis of embryonic cells. Mol Biol Cell 19, 2465–2475.

Kursawe J, Baker RE, Fletcher AG (2017). Impact of implementation choices on quantitative predictions of cell-based computational models. J Comput Phys 345, 752–767.

Ladoux B, Mege RM (2017). Mechanobiology of collective cell behaviours. Nat Rev Mol Cell Biol 18, 743–757.

Letizia A, He D, Astigarraga S, Colombelli J, Hatini V, Llimargas M, Treisman JE (2019). Sidekick is a key component of tricellular adherens junctions that acts to resolve cell rearrangements. Dev Cell 50, 313–326 e315.

Liang X, Michael M, Gomez GA (2016). Measurement of mechanical tension at cell-cell junctions using two-photon laser ablation. Bio-protocol 6, e2068.

Liu Z, Yang Y, Gu A, Xu J, Mao Y, Lu H, Hu W, Lei QY, Li Z, Zhang M (2020). Par complex cluster formation mediated by phase separation. Nat Commun 11, 2266.

Lv Z, Zhang N, Zhang X, Grosshans J, Kong D (2022). The lateral epidermis actively counteracts pulling by the amnioserosa during dorsal closure. Front Cell Dev Biol 10, 865397.

Maartens AP, Wellmann J, Wictome E, Klapholz B, Green H, Brown NH (2016). *Drosophila* vinculin is more harmful when hyperactive than absent, and can circumvent integrin to form adhesion complexes. J Cell Sci 129, 4354–4365.

Manning LA, Perez-Vale KZ, Schaefer KN, Sewell MT, Peifer M (2019). The *Drosophila* Afadin and ZO-1 homologues Canoe and Polychaetoid act in parallel to maintain epithelial integrity when challenged by adherens junction remodeling. Mol Biol Cell 30, 1938–1960.

McGill MA, McKinley RF, Harris TJ (2009). Independent cadherin-catenin and Bazooka clusters interact to assemble adherens junctions. J Cell Biol 185, 787–796.

Müller H-AJ, Wieschaus E (1996). *armadillo*, *bazooka*, and *stardust* are critical for formation of the zonula adherens and maintenance of the polarized blastoderm epithelium in *Drosophila*. J Cell Biol 134, 149–165.

Neel JV (1940). The pattern of supernumerary macrochaetae in certain *Drosophila* mutants. Genetics 25, 251–277.

Oldenburg J, van der Krogt G, Twiss F, Bongaarts A, Habani Y, Slotman JA, Houtsmuller A, Huveneers S, de Rooij J (2015). VASP, zyxin and TES are tension-dependent members of Focal Adherens Junctions independent of the alpha-catenin-vinculin module. Sci Rep 5, 17225.

Ooshio T, Kobayashi R, Ikeda W, Miyata M, Fukumoto Y, Matsuzawa N, Ogita H, Takai Y (2010). Involvement of the interaction of afadin with ZO-1 in the formation of tight junctions in Madin-Darby canine kidney cells. J Biol Chem 285, 5003–5012.

Perez-Vale KZ, Yow KD, Gurley NJ, Greene M, Peifer M (2023). Rap1 regulates apical contractility to allow embryonic morphogenesis without tissue disruption and acts in part via Canoe-independent mechanisms. Mol Biol Cell 34, ar7.

Perez-Vale KZ, Yow KD, Johnson RI, Byrnes AE, Finegan TM, Slep KC, Peifer M (2021). Multivalent interactions make adherens junction–cytoskeletal linkage robust during morphogenesis. J Cell Biol 220, e202104087.

Rauskolb C, Cervantes E, Madere F, Irvine KD (2019). Organization and function of tension-dependent complexes at adherens junctions. J Cell Sci 132, jcs224063.

Rauzi M, Lenne PF, Lecuit T (2010). Planar polarized actomyosin contractile flows control epithelial junction remodelling. Nature 468, 1110–1114.

Razzell W, Bustillo ME, Zallen JA (2018). The force-sensitive protein Ajuba regulates cell adhesion during epithelial morphogenesis. J Cell Biol 217, 3715–3730.

Rodgers LS, Beam MT, Anderson JM, Fanning AS (2013). Epithelial barrier assembly requires coordinated activity of multiple domains of the tight junction protein ZO-1. J Cell Sci 126, 1565–1575.

Rouaud F, Sluysmans S, Flinois A, Shah J, Vasileva E, Citi S (2020). Scaffolding proteins of vertebrate apical junctions: structure, functions and biophysics. Biochim Biophys Acta Biomembr 1862, 183399.

Sarpal R, Pellikka M, Patel RR, Hui FY, Godt D, Tepass U (2012). Mutational analysis supports a core role for *Drosophila* α-catenin in adherens junction function. J Cell Sci 125, 233–245.

Sawyer JK, Choi W, Jung KC, He L, Harris NJ, Peifer M (2011). A contractile actomyosin network linked to adherens junctions by Canoe/afadin helps drive convergent extension. Mol Biol Cell 22, 2491–2508.

Sawyer JK, Harris NJ, Slep KC, Gaul U, Peifer M (2009). The *Drosophila* afadin homologue Canoe regulates linkage of the actin cytoskeleton to adherens junctions during apical constriction. J Cell Biol 186, 57–73.

Schindelin J, Arganda-Carreras I, Frise E, Kaynig V, Longair M, Pietzsch T, Preibisch S, Rueden C, Saalfeld S, Schmid B, *et al.* (2012). Fiji: an open-source platform for biological-image analysis. Nat Methods 9, 676–682.

Schmidt A, Lv Z, Grosshans J (2018). ELMO and Sponge specify subapical restriction of Canoe and formation of the subapical domain in early *Drosophila* embryos. Development 145, dev157909.

Schwayer C, Shamipour S, Pranjic-Ferscha K, Schauer A, Balda M, Tada M, Matter K, Heisenberg CP (2019). Mechanosensation of tight junctions depends on ZO-1 phase separation and flow. Cell 179, 937–952 e918.

Seppa MJ, Johnson RI, Bao S, Cagan RL (2008). Polychaetoid controls patterning by modulating adhesion in the *Drosophila* pupal retina. Dev Biol 318, 1–16.

Sheppard L, Green DG, Lerchbaumer G, Rothenberg KE, Fernandez-Gonzalez R, Tepass U (2023). The α-Catenin mechanosensing M region is required for cell adhesion during tissue morphogenesis. J Cell Biol 222, e202108091.

Simoes SDM, Blankenship JT, Weitz O, Farrell DL, Tamada M, Fernandez-Gonzalez R, Zallen JA (2010). Rho-kinase directs Bazooka/Par-3 planar polarity during Drosophila axis elongation. Dev Cell 19, 377–388.

Sun D, LuValle-Burke I, Pombo-Garcia K, Honigmann A (2022). Biomolecular condensates in epithelial junctions. Curr Opin Cell Biol 77, 102089.

Takahashi K, Matsuo T, Katsube T, Ueda R, Yamamoto D (1998). Direct binding between two PDZ domain proteins Canoe and ZO-1 and their roles in regulation of the jun N-terminal kinase pathway in *Drosophila* morphogenesis. Mech. Dev. 78, 97–111.

Tamada M, Farrell DL, Zallen JA (2012). Abl regulates planar polarized junctional dynamics through β-catenin tyrosine phosphorylation. Dev Cell 22, 309–319.

Tepass U, Gruszynski-DeFeo E, Haag TA, Omatyar L, Török T, Hartenstein V (1996). *shotgun* encodes *Drosophila* E-cadherin and is preferentially required during cell rearrangement in the neurectoderm and other morphogenetically active epithelia. Genes Dev 10, 672–685.

Tepass U, Hartenstein V (1994). The development of cellular junctions in the *Drosophila* embryo. Dev Biol 161, 563–596.

Tetley RJ, Blanchard GB, Fletcher AG, Adams RJ, Sanson B (2016). Unipolar distributions of junctional Myosin II identify cell stripe boundaries that drive cell intercalation throughout *Drosophila* axis extension. eLife 5, 12094.

Troyanovsky SM (2022). Adherens junction: the ensemble of specialized cadherin clusters. Trends Cell Biol 33, 374–387.

Uemura T, Oda H, Kraut R, Hayashi S, Kotaoka Y, Takeichi M (1996). Zygotic *Drosophila* E-cadherin expression is required for processes of dynamic epithelial cell rearrangement in the *Drosophila* embryo. Genes Dev 10, 659–671.

Umeda K, Ikenouchi J, Katahira-Tayama S, Furuse K, Sasaki H, Nakayama M, Matsui T, Tsukita S, Furuse M, Tsukita S (2006). ZO-1 and ZO-2 independently determine where claudins are polymerized in tight-junction strand formation. Cell 126, 741–754.

Utepbergenov DI, Fanning AS, Anderson JM (2006). Dimerization of the scaffolding protein ZO-1 through the second PDZ domain. J Biol Chem 281, 24671–24677.

Xu J, Anuar F, Ali SM, Ng MY, Phua DC, Hunziker W (2009). Zona occludens-2 is critical for blood-testis barrier integrity and male fertility. Mol Biol Cell 20, 4268–4277.

Xu J, Kausalya PJ, Phua DC, Ali SM, Hossain Z, Hunziker W (2008). Early embryonic lethality of mice lacking ZO-2, but Not ZO-3, reveals critical and nonredundant roles for individual zonula occludens proteins in mammalian development. Mol Cell Biol 28, 1669–1678.

Yap AS, Duszyc K, Viasnoff V (2018). Mechanosensing and mechano-transduction at cell–cell junctions. Cold Spring Harb Perspect Biol 10, a028761.

Yu HH, Zallen JA (2020). Abl and Canoe/Afadin mediate mechanotransduction at tricellular junctions. Science 370, eaba5528.

Zallen JA, Wieschaus E (2004). Patterned gene expression directs bipolar planar polarity in *Drosophila*. Dev Cell 6, 343–355.

Zamudio AV, Dall'Agnese A, Henninger JE, Manteiga JC, Afeyan LK, Hannett NM, Coffey EL, Li CH, Oksuz O, Sabari BR, *et al.* (2019). Mediator Condensates Localize Signaling Factors to Key Cell Identity Genes. Genes Mol Cell 76, 753–766.e756.